CLOUD ANALYSIS USING NOAA-7 AVHRR MULTISPECTRAL IMAGERY

by

Robert Paul d'Entremont

B.S. Math., University of Lowell
(1978)

SUBMITTED IN PARTIAL FULFILLMENT
OF THE REQUIREMENTS OF THE
DEGREE OF

MASTER OF SCIENCE
IN METEOROLOGY

at the

MASSACHUSETTS INSTITUTE OF TECHNOLOGY

August 1984

Signature of Author: .....
Department of Earth, Atmospheric, and Planetary Sciences
August 10, 1984

Certified by: .....
Professor Ronald G. Prinn
Thesis Supervisor

Certified by: .....
Theodore Madden
Chairman, Departmental Committee on Graduate Students
Department of Earth, Atmospheric, and Planetary Sciences

Cloud Analysis Using NOAA-7 AVHRR Multispectral Imagery

Contents

CLOUD ANALYSIS USING NOAA-7 AVHRR MULTISPECTRAL IMAGERY

by

Robert Paul d'Entremont

Submitted to the Department of Earth and Planetary Sciences
on August 10, 1984 in partial fulfillment of the
requirements for the Degree of Master of Science in
Meteorology

ABSTRACT

A multispectral low-level nighttime cloud analysis method using NOAA-7 polar orbiter AVHRR imagery is presented. The analysis technique generates cloud amounts and cloud top heights, and is capable of detecting and identifying those parameters for sub-pixel clouds, i.e., for clouds which only partially fill a satellite sensor's field of view. A theoretical satellite-observed radiance model was written for the 3.7μm, 10.7μm, and 11.7μm spectral regions corresponding to the NOAA-7 AVHRR Channels 3, 4, and 5, respectively. Satellite-measured radiances were then compared to the model-predicted radiances to help determine the aforementioned cloud parameters. A wide variety of atmospheric spectral transmission functions for the AVHRR instruments were computed during this study as well. Test cases demonstrated the multispectral cloud analysis method as a useful technique for nighttime imagery analysis.

Thesis Supervisor: Dr. Ronald G. Prinn, Professor of Meteorology

I. Introduction

Meteorological polar-orbiting satellite observations have enabled the determination of many useful physical properties of the Earth's surface and atmosphere by means of remote sensing. Polar orbiter radiometer data provide global coverage of clouds and can therefore be used to analyze cloud top heights and temperatures, fractional cloud cover, and perhaps even reflectivity and emissivity of clouds and surfaces (Wielicki and Coakley, 1981), all on a global basis. Global cloud analysis is recognized to be of fundamental importance to modelers who assess the accuracy of their model's predicted cloud amounts. Climate modelers are very interested in accurate specification of cloud amount, especially low cloud amount (Henderson-Sellers and Hughes, 1983), because of their first order effects on maintaining balanced radiation budgets. An accurate cloud analysis is also necessary to long range modelers since such analyses must be used to assess the validity of model-generated cloud amounts, which in turn play a very important part in cloud/radiation feedback processes.

Many operational automated cloud analyses in use today are essentially single window IR threshold techniques which rely quite heavily on longwave (10 - 12μm) infrared satellite data and reliable surface skin temperatures. Threshold techniques basically compare a satellite-observed brightness temperature to a known underlying surface temperature; if the satellite brightness temperature matches or lies within some predefined range of the surface temperature, the sensor's field of view is considered cloud-free. If on the other hand the satellite brightness temperature is significantly colder than the underlying surface, clouds are considered to lie within the sensor's field of view. Although such

cloud analysis algorithms are computationally quick, there are several instances where and several reasons why they might provide inaccurate results. For example, in the presence of a strong temperature inversion a low cloud could easily be much warmer than the underlying surface. In addition, detection of low clouds at night using an IR radiance threshold technique is usually quite difficult since the IR brightness temperature of the low clouds and of the underlying surface are often very close. Many times the distinction between cloud and surface temperatures is not enough to affect a noticeable change in satellite-measured IR radiances. Regions that appear cloud free in nighttime IR imagery are often completely cloud covered. Yet another problem with single window IR thresholding techniques lies in computing accurate surface and cloud top temperature values. Obstacles are due to the fact that satellite-measured brightness temperatures T_{Br} must generally be corrected for relatively small but nonetheless significant (significant, at least, for thresholding tolerances) atmospheric absorption effects. An atmospheric attenuation correction ΔT must be added to the satellite-measured T_{Br} to obtain a true thermodynamic temperature $T = T_{Br}+\Delta T$. For the most part the ΔT's are empirically estimated, often leading to unreliable surface temperature calculations, especially when atmospheric transmission is low (e.g., as it is for moist, tropical atmospheres or dirty urban atmospheres).

This study presents a cloud analysis technique designed for retrieval of cloud top temperatures and cloud amounts using NOAA-7 Advanced Very High Resolution Radiometer (AVHRR) multispectral imagery. The cloud analysis algorithm was formulated in an effort to overcome some of the aforementioned obstacles that single window IR threshold techniques fre-

quently encounter. Part II describes the cloud analysis theory and application, and presents a description of the NOAA-7 AVHRR and its imagery data characteristics. A brief discussion of other data sources used in this study is also provided. Part III presents the results of some cloud analysis tests, followed by a summary and concluding remarks in Part IV.

II. Cloud Property Analysis Method

A. Remote Sensing of the Earth and Atmosphere

Radiation emitted and reflected by an object on the surface or within the atmosphere interacts with the medium that is present between that object and a satellite sensor. The radiance measured by a sensor is a "signature" which is characteristic of the composition and structure of the target object and the atmosphere that lies within that sensor's field of view. It is in this sense that satellite radiation measurements are used to infer the physical parameters of a target scene and the intervening atmosphere.

Satellite sensors are designed and developed to measure electromagnetic radiation within specific spectral intervals known to be sensitive to some physical aspect of a target or medium. By measuring radiation emitted and reflected within certain spectral regions by the atmosphere and surface below, inferences of atmospheric temperature profiles, aerosol compositions, and water vapor concentrations can be made. Also, cloud top temperature and cloud amount, as well as surface temperatures, can be determined. However, a fundamental problem in determining such characteristics from radiometric measurements lies in the fact that, generally speaking, for a given measured radiance value a number of different combinations of the structure and physical composition of the atmosphere

through which a target's emitted and/or reflected radiation travels will yield that same measured radiance.

There are several optically active gases in a cloud free atmosphere which absorb and reemit thermal radiation in well-defined spectral regions, called absorption bands. Satellite observations of radiation measured within absorption bands generally only see through the top down to middle layers of the atmosphere. These gases block out any radiation at their absorption band wavelengths that originates from atmospheric levels below those where the gases begin to effectively absorb. To derive temperatures through these levels all the way down to the surface, it is necessary that a spectral interval transparent to the effects of all these gases be used. Such intervals are called window regions. Sensors designed for windows "see" through the atmosphere to the underlying surface or cloud top. Several window regions exist throughout the electromagnetic spectrum. Atmospheric windows lie in the following spectral regions: the visible window located around 0.6 - 1.1μm, the near infrared windows at 1.6μm, 2.2μm, and 3.7μm, and the infrared windows at 4.4 - 5.4μm, 8 - 9μm, and 10 - 12μm. A satellite sensor designed for these windows senses for the most part only the radiation emitted by any clouds or the Earth's surface within the sensor's field of view, with relatively little atmospheric contribution. However, for retrievals of almost any physical property using remotely sensed satellite data, the combined effects of radiant energy loss due to molecular absorption and scattering are significant enough that atmospheric attenuation must be accounted for.

B. The NOAA-7 Advanced Very High Resolution Radiometer

A near infrared sensor at the 3.7μm window region was proposed in the late 1960's as a part of the four channel Advanced Very High Resolution Radiometer (AVHRR) flown on the TIROS-N generation of NOAA polar-orbiting satellites. Consequently, the NOAA-7 AVHRR, launched in 1981, was upgraded to a five channel scanning radiometer that senses reflected sunlight (Channels 1 and 2), emitted infrared energy (Channels 4 and 5), and reflected solar/emitted thermal energy (Channel 3) simultaneously in the five window regions listed in Table 1.

There are 2048 samples per channel per AVHRR scan, and each sample step corresponds to an angle of scanner rotation of 0.95 milliradians (Kidwell, 1983). Consequently, the AVHRR has a maximum cross back scan angle of just over 55° from nadir, and each field of view's ground track resolution is 1.1 km at satellite subpoint, decreasing toward the edge of scan. Figure 1 shows where the five AVHRR channels lie in relation to each other on a plot of atmospheric transmittance for a vertical path from ground level to space for the region 0.25 - 28.5μm, and for several atmospheres, as computed by the Air Force Geophysics Laboratory's (AFGL's) LOWTRAN3 atmospheric transmittance/radiance model (Selby and McClatchey, 1975).

Channel 1 responds to reflected solar energy in the visible portion of the spectrum. It is used to detect cloud cover, snow cover, and sea

* * *

Five Channel AVHRR, NOAA-7

Channel 1	Channel 2	Channel 3	Channel 4	Channel 5
0.58 - 0.68μm	0.725 - 1.1μm	3.55 - 3.93μm	10.3 - 11.3μm	11.5 - 12.5μm

Table 1. Spectral intervals for the five NOAA-7 AVHRR window channels (after Lauritson et al., 1979)

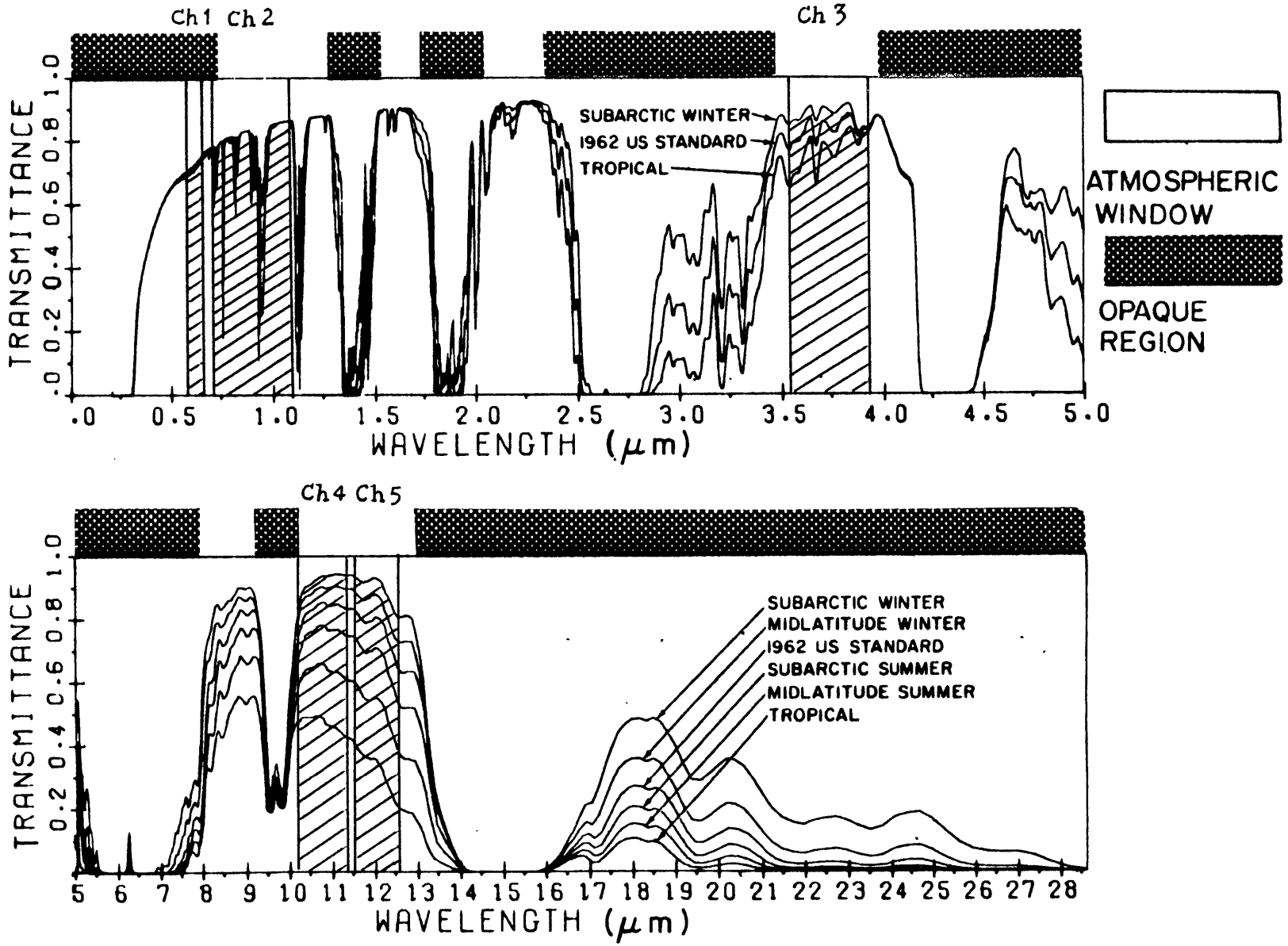

Figure 1. Atmospheric Transmittance for a Vertical Path to Space From Sea Level for Six Model Atmospheres as Computed by LOWTRAN3. The Bandwidths for the Five Channels of the NOAA-7 AVHRR are Indicated (after Selby and McClatchey, 1975)

ice, along with cyclones and even volcanic dust plumes. Channel 2 responds to reflected solar energy in the spectral region 0.7 - 1.1μm. It is good for the same sorts of identifications that Channel 1 is good for, but was added on to the AVHRR because of its differing sensitivity to land backgrounds and water. Most land surfaces reflect near infrared satellite radiation more strongly than visible radiation, so that land/sea boundary features appear much sharper in Channel 2 imagery than they do in Channel 1 imagery.

The infrared Channel 4 is used for thermal mapping of clouds and the Earth's surface and oceans during both day and night, since it is not contaminated by reflected solar radiation. Solar fluxes at such wavelengths are negligibly small. Even though Channel 4 is a window relatively transparent to water vapor (a main tropospheric absorber), tropospheric vapor amounts do cause some attenuation which must generally be accounted for when trying to determine target temperatures (particularly in the tropics and mid-latitude summers). Channel 5 is another infrared region which, as can be seen in Figure 1, is even more sensitive than Channel 4 with respect to water vapor (the transmittances are lower in Channel 5 than they are in Channel 4 for most atmospheres). For dry, clear, cold atmospheres, imagery from both channels looks similar since such atmospheres are comparably clean in any window (in Figure 1 note each channel's respective IR subarctic winter atmosphere transmittances). But due to the atmospheric attenuation effects (primarily of water vapor), moist atmospheres yield Channel 5 brightness temperatures that are cooler than those of Channel 4.

The Channel 3 3.7μm sensor was designed to complement Channel 4's sensor data in the remote sensing of sea surface temperatures (SST's)

by providing corrections for sensor fields of view within which atmospheric water vapor and partial cloud cover exist (McClain, 1981). In the spectral range 3.5 - 3.9μm there is less absorption by water vapor so that energy emitted at 3.7μm by the Earth's surface can penetrate larger column concentrations of water vapor than can energy at the longer IR wavelengths. On the other hand, the AVHRR Channel 3 is sensitive to both reflected solar and emitted terrestrial energy, a characteristic none of the other AVHRR Channels has. Incoming solar radiation is small in comparison to emitted thermal radiation at the longer IR wavelength intervals of Channels 4 and 5 (≈10 - 12μm or so). However at near infrared 3.7μm wavelengths, incident solar radiation is no longer negligible, but can be as large as emitted terrestrial radiation depending on the temperature (Smith and Rao, 1972). In addition, cloud reflectivities at 3.7μm can approach 30% (see Figure 2), so that reflected sunlight can easily be a significant part of daytime 3.7μm radiance measurements. For this reason, the use of Channel 3 data has historically been restricted largely to nighttime applications.

C. Daytime Characteristics of AVHRR Imagery

The AVHRR imagery in Figures 3a, 3b, and 3c were taken simultaneously in daylight hours over the Arctic Ocean. The Channel 2 imagery of Figure 3a is shown here instead of the Channel 1 imagery because boundaries of water with other surfaces contrast more sharply in the Channel 2 spectral range 0.725 - 1.1μm, as previously mentioned. Even though some of Channel 2 is technically outside the "visible" part of the spectrum, its characteristics for the most part resemble those of the Channel 1 visible band. Thus during the following discussion Channel 2 imagery may be referred to

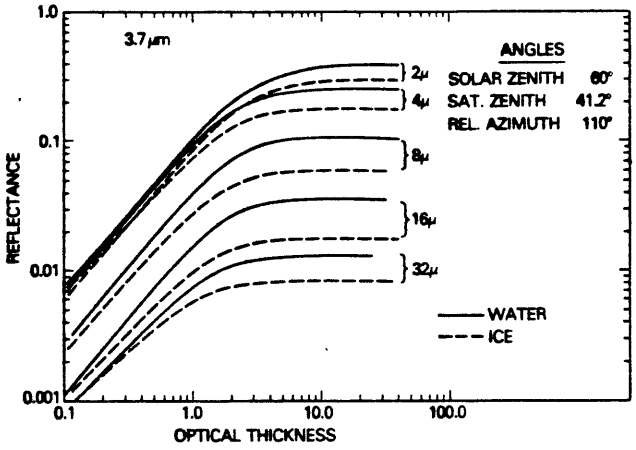

Figure 2. Theoretical Calculations of the Reflectance at 3.7μm Versus Optical Thickness for Plane Parallel Clouds With Various Particle Sizes and Thermodynamic Phase (from Arking and Childs, 1983)

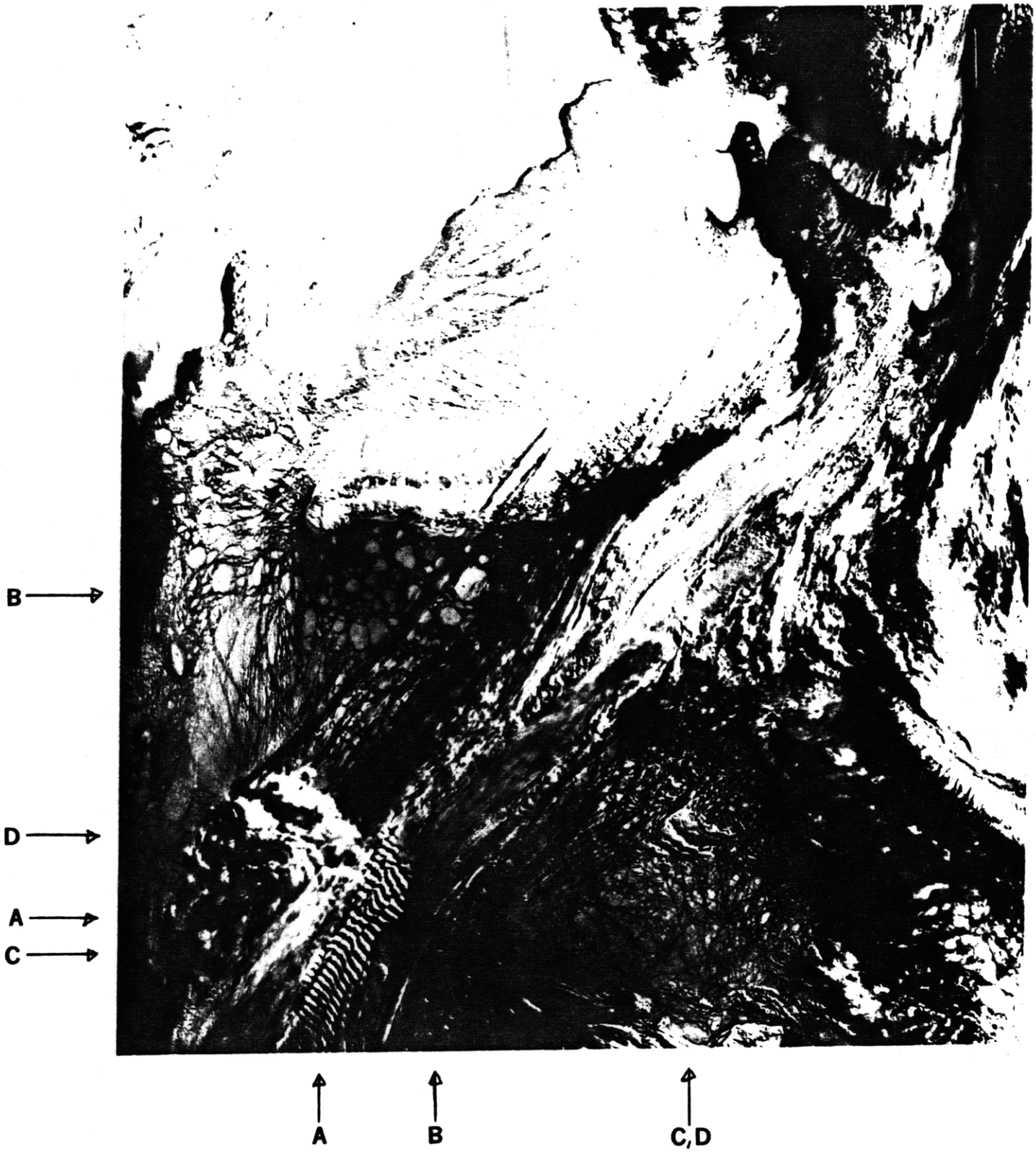

Figure 3a. NOAA-7 AVHRR Channel 2 (0.725 - 1.1μm) Imagery of Novaya Zemlya in the Arctic Ocean

Figure 3b. NOAA-7 AVHRR Channel 3 (3.55 - 3.93μm) Imagery of Novaya Zemlya in the Arctic Ocean

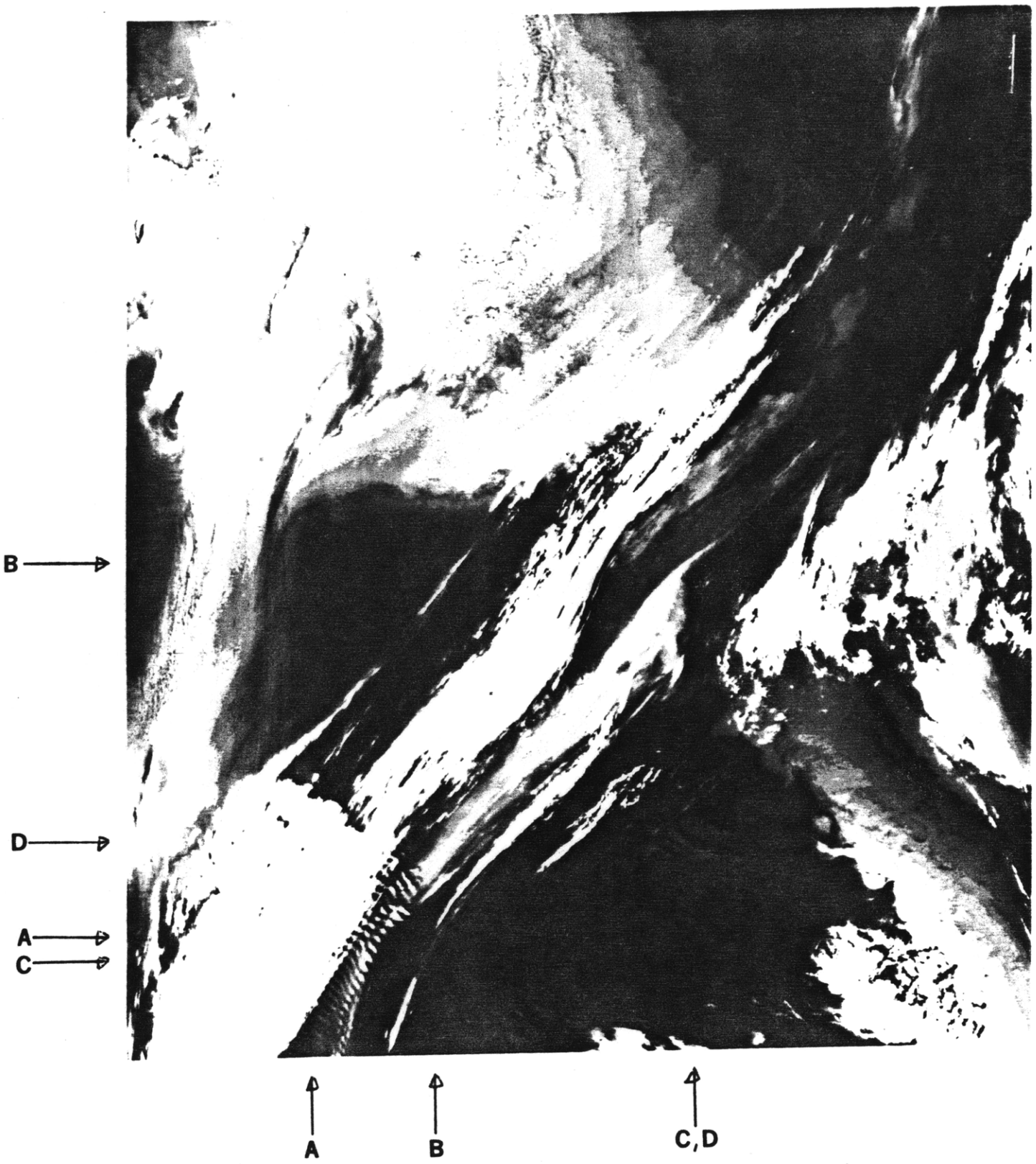

Figure 3c. NOAA-7 AVHRR Channel 4 (10.3 - 11.3μm) Imagery of Novaya Zemlya in the Arctic Ocean

as "visible" imagery.

Bright tones in Figure 3a denote high albedos (e.g., clouds, snow/ice covered land), while darker tones denote lower albedos (e.g., ice free surfaces, forests). Black is open ocean. The Channel 4 IR imagery is shown in Figure 3c. Cold temperatures are represented by bright tones and warm temperatures by dark. At nighttime, the tones of gray in Channel 3 imagery would exhibit the same general characteristics as the imagery of Channel 4, i.e. cold is bright and warm is dark. In daytime, reflected incident solar radiation contaminates this scheme, as can be seen in comparing Figure 3c with Figure 3b.

Note most obviously that the 3.7μm imagery is not always dark (hot) where the 11μm imagery is dark. Likewise, the two imagery types are not always correspondingly bright (cold). At night, in the absence of any solar radiation, the 3.7 and 10.7μm images would look characteristically similar.

The point A denotes an area of high, cold (bright in the IR) cirrus clouds. Their ripples and shadows can be detected in the visible, and even in the IR a hint of their wavelike structure is noticeable. In the IR these clouds appear to be colder than just about any other cloud or land feature in the image, but this is not so in the near IR image 3b. In fact the point A appears considerably warmer in the near infrared image than does point B, in direct contradiction to the IR image information. As can be seen in the visible image, point B contains an area of sea ice and open ocean. The ice free ocean should be much warmer than the high cirrus cloud tops. This opinion is substantiated by the fact that in the IR window (3c), which is not directly affected by reflected solar radiation, the cirrus tops are indeed brighter and therefore colder than

both the open ocean and the sea ice areas. The reason that the near infrared image has "inverted" this scheme is because at 3.7μm, liquid water and ice/snow are good absorbers of incident solar radiation. Thus the water and ice don't reflect as much 3.7μm incident solar radiation back to space as the nonwater bodies around it do, in turn making it look colder in relation to everything around it. The cirrus clouds of region A on the other hand reflect a much more significant part of incident 3.7μm solar radiation back to space (note the Figure 2 reflectances for ice particle clouds), giving them warmer brightness temperatures than the truly warmer water below. It should be kept in mind that the appearance of thin cirrus clouds in nearly any spectral region is based not only on what it reflects or emits at a given wavelength, but also is further complicated by the fact that thin cirrus transmissivities are significant. In other words, some of the radiation emitted by the surfaces below pass directly through the thinner parts of ice clouds, changing the appearances of these surfaces noticeably.

The cloud free, snow covered area surrounding point C illustrates a similar phenomenon. The snow effectively absorbs all of the incoming 3.7μm solar radiation, so that it does not appear warm in the Channel 3 image as the Channel 4 image shows it to be. Note also the midlevel water droplet cloud D. It appears warmer in the 3.7μm image than does the surface beneath it, whereas the more truly temperature-representative 10.7μm image shows the cloud to be significantly cooler than the ground below. Water droplets reflect better at 3.7μm than ice crystals do (see Figure 2). The 3.7μm reflectivities of ice crystals and water droplets are an interesting property; intercomparison of a 3.7μm daytime image with a corresponding 10.7μm image helps to discriminate water clouds (and

ice clouds) from from underlying snowy backgrounds. Such discriminations on the basis of visible and thermal IR imagery alone can often be quite difficult.

In these images there are more illustrations of the problems encountered when dealing with daytime Channel 3 radiance data. Separating out reflected solar from thermal emissive effects at 3.7μm during daylight hours is not a trivial task. Corrections for reflected solar radiation at 3.7μm are highly variable functions of surface properties and scene solar elevation angle, and comprise a whole study in themselves. It is for this reason that this multispectral image analysis study restricts itself to the use of nighttime Channel 3 AVHRR data.

D. Infrared Atmospheric Radiation Physics

The monochromatic upwelling thermal radiance at the top of a non-scattering, plane-parallel, cloud-free atmosphere, which is in local thermodynamic equilibrium and whose source function is the Planck function, may be written as a function of pressure p at the top of the atmosphere (where p=0) in the form (Liou, 1980)

$$I_\lambda(0) = I_\lambda(p_{sfc})\,\mathcal{T}_\lambda(p_{sfc}) + \int_{p_{sfc}}^{0} B_\lambda[T(p)]\frac{\partial\,\mathcal{T}_\lambda(p)}{\partial p}dp, \qquad (1)$$

where $\mathcal{T}_\lambda$ is the monochromatic transmission function for wavelength λ and is often called transmittance, and where B_λ is the Planck emission for a blackbody of temperature T. The subscript sfc denotes surface values. The transmission function $\mathcal{T}_\lambda(p)$ is

$$\mathcal{T}_\lambda(p) = \exp(-\tau_\lambda(p)), \qquad (2)$$

and the optical depth τ_λ is defined

$$\tau_\lambda(p) = \sum_{gases}\{-\frac{1}{g}\int_p^0 k_\lambda(p')\frac{\rho}{\rho_{air}}(p')dp'\}, \qquad (3)$$

where k_λ is the absorption coefficient (in units of effective cross-sectional absorbing area per unit mass of absorbing gas $[L^2M^{-1}]$), ρ and ρ_{air} are the densities of the absorbing gas and the atmosphere, respectively, and g is the acceleration of gravity. Optical depth is never negative; since the integrand on the right side of (3) is positive definite (both k_λ and ρ/ρ_{air} are nonnegative by definition), the order of integration in (3) ensures τ to be positive as well. Since $\tau \geq 0$, then from (2) it is easily seen that transmittance $\mathcal{T}_\lambda$ is always within the range $0 < \mathcal{T}_\lambda \leq 1$. The lower the transmittance, the more opaque the atmospheric path is to radiation of wavelength λ. The cleaner or more transparent an atmospheric path is for a particular wavelengths's radiation, the smaller the value of the optical depth and the larger the transmittance. Thus near the top of the atmosphere ($p \to 0$) where there exist virtually no absorbing gases or aerosols, optical depth $\tau \to 0$ as well. As the path length through the atmosphere increases then so too does optical depth, in general. The less transparent (more opaque) an atmosphere becomes, the larger τ becomes. $\mathcal{T}_\lambda(p_{sfc}) = \exp(-\tau_\lambda(p_{sfc}))$ is usually significantly less less than 1; at the top of the atmosphere, $\mathcal{T}_\lambda(p=0) = \exp(-\tau_\lambda(p=0)) = e^{-0} = 1$. In short, the transmittance is a measure of the fraction of radiant emission from a body that makes it through the atmosphere and out to space.

The quantity $\frac{\partial \mathcal{T}_\lambda(p)}{\partial p}$ on the right side of equation (1) can be regarded as a weighting function. It is a wavelength and pressure (height) dependent function which, when multiplied by the Planck emission, gives the atmospheric contribution of level z(p) to the upwelling radiance $I_\lambda(0)$. Figure 4 shows a qualitative example of what corresponding atmospheric transmittances and weighting functions look like. The peak in the weighting function curves indicates where within the atmosphere originate the most significant contributions to measured upwelling radiance. It can be shown that the levels of these peaks are given by

$$z_{peak} = H\ell n\tau_{\lambda,sfc},$$

where $\tau_{\lambda,sfc}$ is the cloud free atmospheric optical depth from space to ground level, and where H is the scale height of the particular band absorber (Prinn, course notes). This peak lies at the level z where optical depth $\tau_\lambda(z)$ from the top of the atmosphere to z is approximately unity. Hence in window regions such as those of the NOAA-7 AVHRR where optical depth is small (i.e., <1), weighting functions attain their largest values at the surface. On the other hand, in spectral regions where optical depth is significantly larger (i.e., >1; large optical depths are due to absorption by such gases as water vapor, ozone, and carbon dioxode), then the corresponding weighting functions peak at levels z_{peak} above the surface. Observations of radiation measured within absorption bands generally only see through the top down to middle layers of the atmosphere, since absorbing gases block out any radiation at their absorption band wavelengths that originates from levels below those where the gases begin to effectively absorb. Figure 4 shows weighting functions for two absorption bands with peaks at 50 mb and 400 mb, and also shows a weighting function for a "dirty" window which peaks at the surface. In summary, the quicker

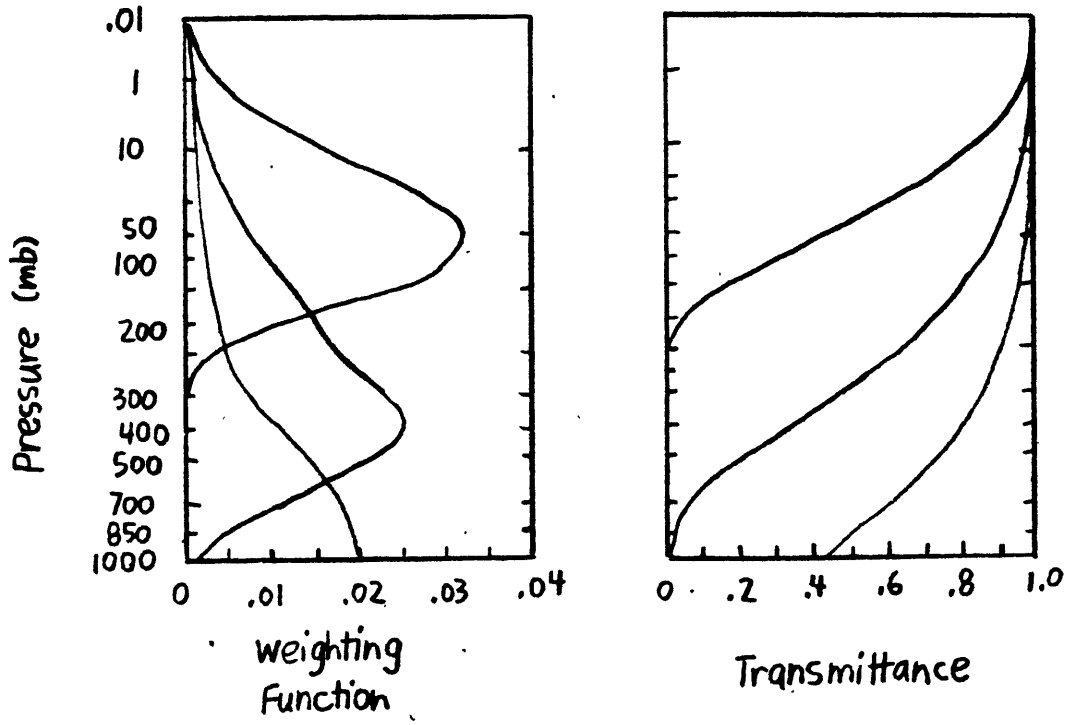

Figure 4. Qualitative Example of Transmittances and Corresponding Weighting Functions (after Liou, 1980)

with height the transmittance for a particular wavelength approaches unity, the further through the atmosphere a satellite sensor responsive to energy at that wavelength can see.

The term $I_\lambda(p_{sfc})$ in equation (1) represents emitted surface radiance, and is given by

$$I_\lambda(p_{sfc}) = \varepsilon_\lambda B_\lambda(T_{sfc}), \qquad (4)$$

where ε_λ is the emissivity of the emitting surface. Emissivity is the relative emissive power of a radiating surface expressed as a fraction of the emissive power of a blackbody radiator at the same temperature. Emissivity is a function of both wavelength and surface (e.g., rocks, trees, ice crystals, water droplets).

Equation (4) implies that there is no incident solar radiation of wavelength λ reflected back out to the atmosphere by the surface, and likewise that there is no downward-reflected atmospheric contribution of radiation at wavelength λ which might be reflected back out by the surface. Also, (4) is valid for surfaces with zero reflectivities at wavelength λ. In any event, (4) is certainly valid for the AVHRR window regions at night, when incident solar fluxes which might affect Channel 3 are nonexistent.

Substituting the form (4) for $I_\lambda(p_{sfc})$ into (1), the following expression for $I_\lambda(0)$ is obtained:

$$I_\lambda(0) = \varepsilon_\lambda B_\lambda(T_{sfc})\,\mathcal{T}_\lambda(p_{sfc}) + \int_{p_{sfc}}^{0} B_\lambda[T(p)]\frac{\partial \mathcal{T}_\lambda(p)}{\partial p}dp. \qquad (5)$$

Equation (5) gives a form in pressure coordinates for the upwelling thermal radiance at a single (monochromatic) wavelength. However, spaceborne satellite sensors are designed to measure radiant energies within

some wavelength range (λ_1,λ_2). The observed upward spectral radiance I_{λ}^{obs} sensed by a downward pointing radiometer in band width (λ_1,λ_2) (call this band width Channel j, say) is a weighted average of the monochromatic radiances $I_\lambda(0)$ (from (5)), and is given by

$$I_{\bar{\lambda}}^{obs,j}(0) = \frac{\int_0^\infty I_\lambda(0)R_j(\lambda)d\lambda}{\int_0^\infty R_j(\lambda)d\lambda} \quad , \qquad (6)$$

where $R_j(\lambda)$ is the response function for channel j, and $\bar{\lambda}$ is the central wavelength in the band width (λ_1,λ_2). $\bar{\lambda}$ is a function $\bar{\lambda}_j$ of channel j. The response function $R_j(\lambda)$ takes on values between 0 and 1, and is often expressed in percent. $R_j(\lambda)$ is a measure of Channel j's sensor response to radiation at wavelength λ; if $R_j(\lambda)$ is 1, the sensor detects 100% of the energy radiated at wavelength λ, whereas if $R_j(\lambda)$ is .89, then the sensor only detects 89% of the total energy radiated at wavelength λ. Sensors are designed to have response functions $R_j(\lambda)$ that are zero outside some wavelength range (λ_1,λ_2); within this range it is generally a rapidly varying function of wavelength. Response functions are usually depicted in graphical or tabular form. They are predetermined by the instrument manufacturer according to customer needs and the properties of the sensor optical components. The response functions for the five NOAA-7 AVHRR Channels 1, 2, 3, 4, and 5 are shown in Figure 5.

The spectral radiance $I_{\bar{\lambda}}^{obs}(0)$ measured by a satellite sensor is given by equation (6), with $I_\lambda(0)$ as given by equation (5). The Planck radiance $B_\lambda(T)$ is

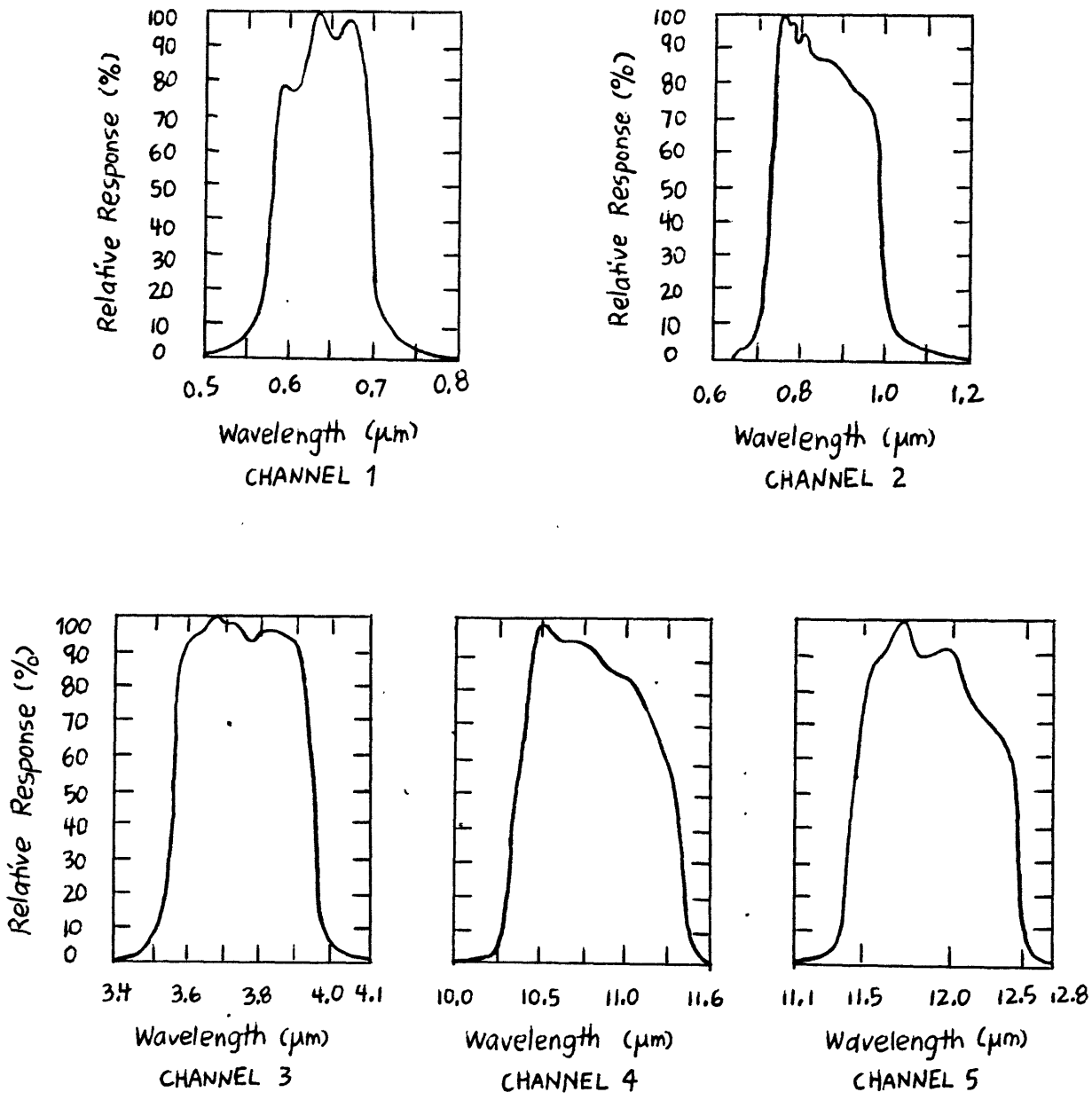

Figure 5. Response Functions for the NOAA-7 AVHRR Window Channels 1-5 (from Kidwell, 1983)

$$B_\lambda(T) = \frac{2hc^2}{\lambda^5} \cdot \frac{1}{\exp(hc/\lambda kT)-1}, \qquad (7)$$

where $h = 6.63 \times 10^{-27}$ erg sec photon^{-1} is Planck's constant, $c = 3 \times 10^{10}$ cm sec^{-1} is the speed of light, and $k = 1.38 \times 10^{-16}$ erg $^{o}K^{-1}$ molecule^{-1} is Boltzmann's constant. The brightness temperature, or equivalent blackbody temperature, is defined as

$$T_{Br} = \frac{hc}{\lambda k} \frac{1}{\ln(2hc^2/\lambda^5 B_\lambda + 1)}, \qquad (8)$$

and corresponds to the temperature a blackbody would have if it emits radiation at an intensity $B_\lambda(T_{Br})$. When satellite-measured radiances are inverted to obtain brightness temperatures using $I_{\bar{\lambda}}^{obs}$ in place of B_λ in equation (8), for most objects the temperatures T_{Br} thus obtained are not true thermodynamic temperatures. They are generally lower than actual, due primarily to atmospheric attenuation effects and surface emissivity properties.

Substituting the form (5) for $I_\lambda(0)$ into (6) yields

$$I_{\bar{\lambda}}^{obs,j}(0) = \frac{1}{\int_0^\infty R_j(\lambda)d\lambda} \left[\int_0^\infty \{\varepsilon_\lambda B_\lambda(T_{sfc})\, \mathcal{T}_\lambda(p_{sfc}) + \int_{p_{sfc}}^0 B_\lambda[T(p)] \frac{\partial \mathcal{T}_\lambda(p)}{\partial p} dp\} R_j(\lambda)d\lambda \right]. \qquad (6b)$$

Since the response function $R_j(\lambda)$ is identically zero outside some spectral interval $\lambda_{j,1} < \lambda < \lambda_{j,2}$, then note that the $\int_0^\infty d\lambda \rightarrow \int_{\lambda_{j,1}}^{\lambda_{j,2}} d\lambda$ in equation (6) and in the equation above since

$$R_j(\lambda) = \begin{cases} 0 & \lambda<\lambda_{j,1} \text{ or } \lambda>\lambda_{j,2} \\ \leq 1 & \lambda_{j,1}\leq\lambda\leq\lambda_{j,2}. \end{cases}$$

The above equation for $I_{\bar{\lambda}}^{obs}(0)$ can then be written

$$I_{\bar{\lambda}}^{obs,j}(0) = \frac{1}{\int_{\lambda_{j,1}}^{\lambda_{j,2}} R_j(\lambda)d\lambda}\left[\int_{\lambda_{j,1}}^{\lambda_{j,2}}\left\{\varepsilon_\lambda B_\lambda(T_{sfc})\mathcal{T}_\lambda(p_{sfc}) + \int_{p_{sfc}}^{0} B_\lambda[T(p)]\frac{\partial \mathcal{T}_\lambda(p)}{\partial p}dp\right\}R_j(\lambda)d\lambda\right]$$

$$= \frac{1}{\int_{\lambda_{j,1}}^{\lambda_{j,2}} R_j(\lambda)d\lambda}\left[\int_{\lambda_{j,1}}^{\lambda_{j,2}}\varepsilon_\lambda B_\lambda(T_{sfc})\mathcal{T}_\lambda(p_{sfc})R_j(\lambda)d\lambda + \int_{\lambda_{j,1}}^{\lambda_{j,2}}\int_{p_{sfc}}^{0} B_\lambda[T(p)]\frac{\partial \mathcal{T}_\lambda(p)}{\partial p}dp\,R_j(\lambda)d\lambda\right] . \quad (9)$$

Now if the spectral region $\lambda_1\leq\lambda\leq\lambda_2$ is sufficiently small that $B_\lambda(T)$ varies slowly with wavelength $\lambda\in[\lambda_1,\lambda_2]$, then B_λ may be replaced with $\bar{B}_j(T)$ to a good approximation (in other words, the variation with wavelength of B_λ is small and smooth over the interval $\lambda_1\rightarrow\lambda_2$ and hence B_λ can be effectively removed from inside the $\int d\lambda$ in the first term on the right side of equation (9)). Assuming similarly that $\varepsilon_\lambda B_\lambda(T_{sfc}) \rightarrow \overline{\varepsilon_j B_j}(T_{sfc})$ (for most earth surfaces, ε_λ is relatively independent of λ over the range of an AVHRR channel (Dozier, 1981)), then equation (9) can be written

$$I_{\bar{\lambda}}^{obs,j}(0) \cong \frac{1}{\int_{\lambda_{j,1}}^{\lambda_{j,2}} R_j(\lambda)\,d\lambda}\left[\overline{\varepsilon_j B_j}(T_{sfc})\int_{\lambda_{j,1}}^{\lambda_{j,2}}\mathcal{T}_\lambda(p_{sfc})R_j(\lambda)d\lambda + \int_{\lambda_{j,1}}^{\lambda_{j,2}}\int_{p_{sfc}}^{0} B_\lambda[T(p)]\frac{\partial \mathcal{T}_\lambda(p)}{\partial p}dp\,R_j(\lambda)\,d\lambda\right], \quad (10)$$

where the overbar "—" is defined as some average wavelength operator over the interval $\lambda_{j,1}<\lambda<\lambda_{j,2}$. Now consider the double integral term $\int\int dp d\lambda$ on the right side of (10). Reversing the order of integration in this term gives

$$\int_{\lambda_{j,1}}^{\lambda_{j,2}} \int_{P_{sfc}}^{0} B_\lambda[T(p)] \frac{\partial \mathcal{T}_\lambda(p)}{\partial p} dp\, R_j(\lambda) d\lambda = \int_{P_{sfc}}^{0} \int_{\lambda_{j,1}}^{\lambda_{j,2}} B_\lambda[T(p)] \frac{\partial \mathcal{T}_\lambda(p)}{\partial p} R_j(\lambda) d\lambda\, dp \ .$$

Again invoking the assumption that the variation of $B_\lambda(T)$ with respect to wavelength λ is small and smooth over the interval $\lambda_{j,1}<\lambda<\lambda_{j,2}$, the above becomes

$$= \int_{P_{sfc}}^{0} \bar{B}_j[T(p)] \int_{\lambda_{j,1}}^{\lambda_{j,2}} \frac{\partial \mathcal{T}_\lambda(p)}{\partial p} R_j(\lambda) d\lambda\, dp \ .$$

Substitution of the above form for the $\int\int dp d\lambda$ term in (10) yields

$$I_{\bar{\lambda}}^{obs,j}(0) \cong \frac{1}{\int_{\lambda_{j,1}}^{\lambda_{j,2}} R_j(\lambda) d\lambda} \left[\overline{\varepsilon_j B_j}(T_{sfc}) \int_{\lambda_{j,1}}^{\lambda_{j,2}} \mathcal{T}_\lambda(P_{sfc}) R_j(\lambda) d\lambda + \int_{P_{sfc}}^{0} \bar{B}_j[T(p)] \int_{\lambda_{j,1}}^{\lambda_{j,2}} \frac{\partial \mathcal{T}_\lambda(p)}{\partial p} R_j(\lambda) d\lambda\, dp \right] . \qquad (11)$$

Defining the <u>spectral transmittance</u> $\mathcal{T}_{\bar{\lambda}_j}(p)$ as

$$\mathcal{T}_{\bar{\lambda}_j}(p) = \frac{\int_{\lambda_{j,1}}^{\lambda_{j,2}} \mathcal{T}_\lambda(p) R_j(\lambda) d\lambda}{\int_{\lambda_{j,1}}^{\lambda_{j,2}} R_j(\lambda) d\lambda} , \qquad (12a)$$

and the spectral weighting function $\frac{\partial \mathcal{T}_{\bar{\lambda}_j}(p)}{\partial p}$ as

$$\frac{\partial \mathcal{T}_{\bar{\lambda}_j}(p)}{\partial p} = \frac{\int_{\lambda_{j,1}}^{\lambda_{j,2}} \frac{\partial \mathcal{T}_{\lambda}(p)}{\partial p} R_j(\lambda) d\lambda}{\int_{\lambda_{j,1}}^{\lambda_{j,2}} R_j(\lambda) d\lambda}, \qquad (12b)$$

then (11) can be written in the simpler form

$$I_{\bar{\lambda}}^{obs,j}(0) \cong \overline{\varepsilon_j B_j}(T_{sfc}) \mathcal{T}_{\bar{\lambda}_j}(p_{sfc}) + \int_{p_{sfc}}^{0} \bar{B}_j[T(p)] \frac{\partial \mathcal{T}_{\bar{\lambda}_j}(p)}{\partial p} dp. \qquad (13)$$

Both the spectral transmittance (12a) and the spectral weighting function (12b) take into account the sensor response function $R_j(\lambda)$. Note the similarity of the form of equation (13) to that of equation (5).

Equation (13) gives the form for satellite-observed radiances. However, keep in mind that the form (13) for $I_{\bar{\lambda}}^{obs}(0)$ is an approximation to the exact form (6) for two reasons. First of all the Planck emittance $B_\lambda(T)$, along with the surface emission $\varepsilon_\lambda B_\lambda(T_{sfc})$, was considered essentially independent of wavelength for a given spectral region $\lambda_1 < \lambda < \lambda_2$, as previously stated. This is not a bad assumption at all for "small" spectral intervals, but the NOAA-7 AVHRR spectral intervals are not so small as to constrain $B_\lambda(T)$ to be precisely constant within them. For typical terrestrial temperatures, the approximation $B_\lambda(T) \rightarrow \bar{B}_j(T)$ (remember that even the average $\bar{B}_j$ is still a function of λ (i.e., a function of Channel number)) is better for the longer IR wavelength AVHRR channels than it is for the shorter ones, as is depicted in Table 2. Variations of blackbody radiances for the 3.7μm Channel 3 sensor are on the order of one order of magnitude, whereas they are more consistent for the wavelengths

	Lower bound of $R_j(\lambda)$ (in μm)	$B_\lambda(273\ ^oK)$ (Watts m^{-2} μm^{-1} $ster^{-1}$)	Upper bound of $R_j(\lambda)$ (in μm)	$B_\lambda(273\ ^oK)$ (Watts m^{-2} μm^{-1} $ster^{-1}$)
Channel 3	3.442	.055236	4.142	.291088
Channel 4	10.0	6.156901	11.65	6.086909
Channel 5	11.1	6.181713	12.8	5.739613

Table 2. Values of Planck blackbody radiances at 273 ^oK for the lower and upper wavelength bounds of the response functions for NOAA-7 AVHRR Channels 3, 4, and 5

in the Channel 4 and 5 regions. In addition, it must be remembered that the response functions R for each of the three channels listed in Table 2 are small for some of the wavelengths for which they are defined. In light of these consequences, the choice of the definition for $\overline{B}_j(T)$ should be made with care and caution, especially when using (13) to theoretically estimate upwelling thermal radiances observed by the AVHRR Channel 3 sensor.

Second, the emissivities ε_λ were also considered independent of λ for $\lambda_1 < \lambda < \lambda_2$. However, the assumption $\varepsilon_\lambda \to \overline{\varepsilon}_j$ turns out to be far better than the assumption $B_\lambda \to \overline{B}_j$, since emissivities don't change much over spectral intervals like those of the AVHRR. It is far more a problem to be able to accurately specify the emissivities ε_λ as a function of varying surface types such as vegetation, forests, snow, and water.

The form (13) for $I_{\overline{\lambda}}^{obs}(0)$ is more desirable than the form (6b) as far as numerical integration techniques are concerned. Equation (6b) contains a double integral term $\int\int_{\lambda p} dp d\lambda \to \sum_n \sum_m \Delta p_m \Delta\lambda_n$, whereas equation (13) contains at most a single integration $\int dp \to \sum_m \Delta p_m$. However, recall that the reduction in computational iterations offered by (13) is gained at the expense of the two approximations $B_\lambda(T) \to \overline{B}_j(T)$ and $\varepsilon_\lambda B_\lambda(T_{sfc}) \to \overline{\varepsilon_j B_j}(T_{sfc})$ and the subsequent associated reductions in the accuracy of the computed radiances.

E. Cloud Property Retrieval Method

Equation (13) for the satellite-observed radiances can be written in pressure coordinates (at the top of the atmosphere, p=0):

$$I_{\bar{\lambda}}^{obs,j}(0) \cong \overline{\varepsilon_j B_j}(T_{sfc})\,\mathcal{T}_{\bar{\lambda}_j}(p_{sfc}) + \int_{p=p_{sfc}}^{0} \bar{B}_j[T(p)]\,\frac{\partial \mathcal{T}_{\bar{\lambda}_j}(p)}{\partial p}\,dp, \quad (13a)$$

in height coordinates (at the top of the atmosphere, z=∞):

$$I_{\bar{\lambda}}^{obs,j}(\infty) \cong \overline{\varepsilon_j B_j}(T_{sfc})\,\mathcal{T}_{\bar{\lambda}_j}(0) + \int_{z=0}^{\infty} \bar{B}_j[T(z)]\,\frac{\partial \mathcal{T}_{\bar{\lambda},j}(z)}{\partial z}\,dz \quad (13b)$$

or in transmission coordinates (at the top of the atmosphere, λ=1):

$$I_{\bar{\lambda}}^{obs,j}(1) \cong \overline{\varepsilon_j B_j}(T_{sfc})\,\mathcal{T}_{\bar{\lambda}_j,sfc} + \int_{\mathcal{T}_{\bar{\lambda}_j,sfc}}^{1} \bar{B}_j[T(\mathcal{T}_{\bar{\lambda}_j})]\,d\mathcal{T}_{\bar{\lambda}_j}. \quad (13c)$$

Each of the three equations (13a) - (13c) yield exactly the same radiances for the continuous vertical grid case. However when they are approximated in quadrature form, different $I_{\bar{\lambda}}^{obs}$ values may be obtained for each of the three vertical coordinate systems. The following example illustrates this point.

Recall that the form (2) for the transmission, which shows the transmission function to be logarithmic in nature. Recall, too, that for atmospheric windows the transmission function takes on its lowest values at the surface and monotonically increases upward with height. With these facts in mind, consider now the qualitative plots of a window transmission function versus two of the three aforementioned vertical coordinates, namely pressure and height, as drawn in Figure 6.

Assume a simple five layer quadrature for the equations (13a) and

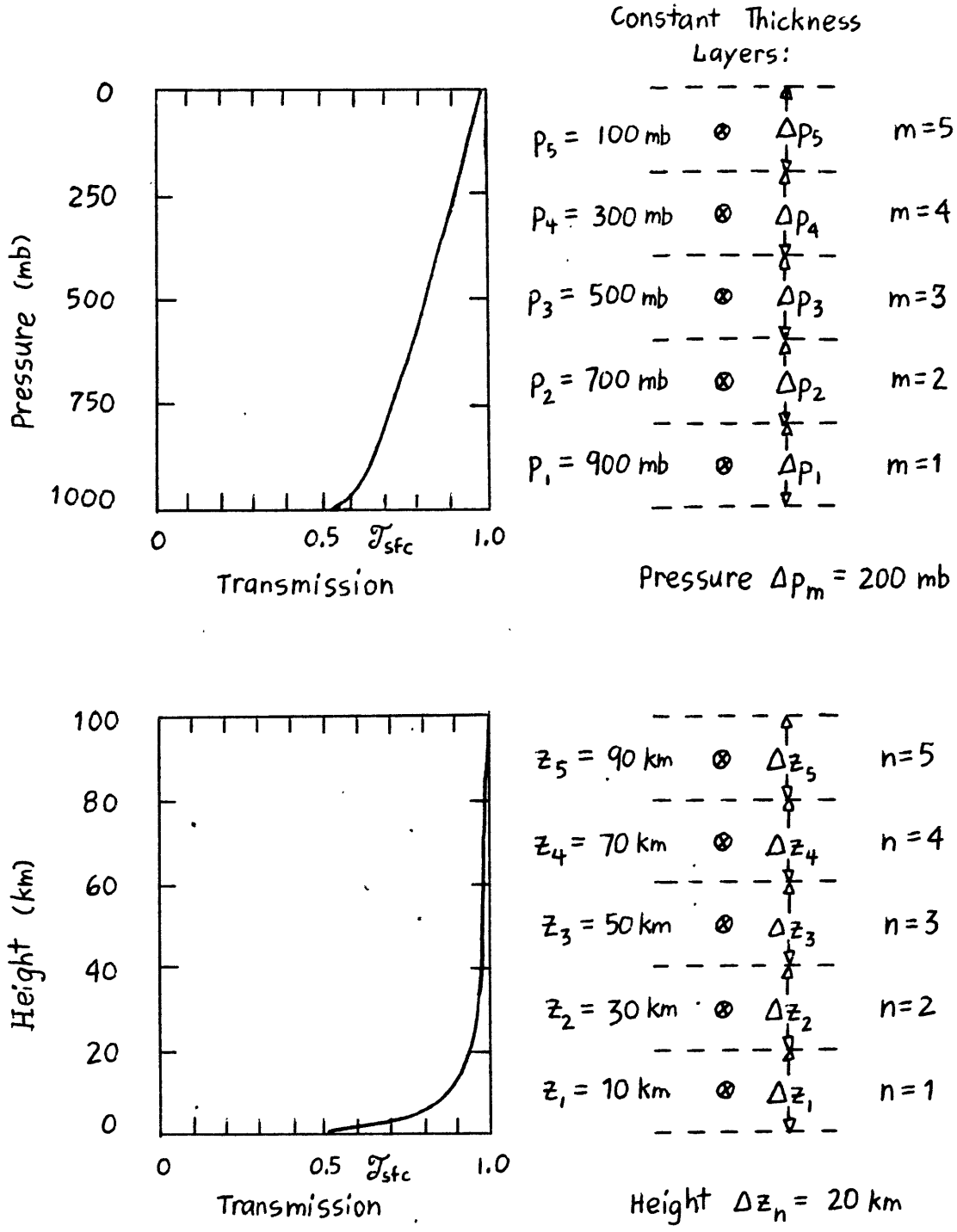

Figure 6. A Qualitative Plot of the Transmission Function for a Typical Window Region, Graphed Versus Pressure and Height as Vertical Coordinates

(13b), respectively, as follows:

$$I_{\bar{\lambda}}^{obs,j}(0) \cong \overline{\varepsilon_j \bar{B}_j}(T_{sfc})\,\mathcal{T}_{\bar{\lambda}}(p_{sfc}) + \sum_{m=1}^{5} \bar{B}_j(T_m)\,P_m\,\Delta p_m \ , \qquad (14a)$$

where $P_m \equiv \left.\frac{\partial \mathcal{T}}{\partial p}\right|_{p=p_m}$ is the pressure coordinate weighting function, and

$$I_{\bar{\lambda}}^{obs,j}(\infty) \cong \overline{\varepsilon_j \bar{B}_j}(T_{sfc})\,\mathcal{T}_{\bar{\lambda}}(0) + \sum_{n=1}^{5} \bar{B}_j(T_n)\,Z_n\,\Delta z_n \ , \qquad (14b)$$

where $Z_n \equiv \left.\frac{\partial \mathcal{T}}{\partial z}\right|_{z=z_n}$ is the height coordinate weighting function. For the above hypothetical case, the layer thicknesses Δp_m for the pressure coordinate quadrature are given by

$$\Delta p_m = \frac{p_{sfc} - 0}{5} \cong 200 \text{ mb},$$

and the layer centers p_m are 900, 700, 500, 300, and 100 mb. The layer thicknesses Δz_n for the height coordinate quadrature are given by

$$\Delta z_n = \frac{100 \text{ km} - 0 \text{ km}}{5} \cong 20 \text{ km},$$

and the layer centers z_n are 10, 30, 50, 70, and 90 km. In the altitude case note that at least 4 out of 5 of the layer centers lie in atmospheric regions where the transmissions are quite close to one. The atmospheric contribution to upwelling thermal radiance is very small in these regions, i.e., is very small from levels with transmittances close to 1, since temperatures are quite cold and absorption by constituents in atmospheric window regions is small. Hence, 4 out of the 5 quadrature points in the vertical grid for equation (14b) add essentially no contribution to $I_{\bar{\lambda}}^{obs}$.

Clearly the bulk of the atmospheric window contribution to $I_{\bar{\lambda}}^{obs}$ comes from

the lowest atmospheric levels where tropospheric window absorber concentrations (mainly water vapor) are highest and temperatures are usually warmest. The pressure coordinates (equation (14a)) are clearly superior to the altitude coordinates but still they are not optimal. Indeed, unlike the layers depicted in Figure 6, it would be advantageous to choose a radiance quadrature scheme the majority of whose layers' centers lie at levels much closer to the ground. Choosing layers of equal transmittance thickness alleviates this finite layer quadrature problem in the best possible way.

The five layer equal transmittance quadrature for (13c) can be written

$$I_{\bar{\lambda}}^{obs,j}(1) \cong \overline{\epsilon_j B_j}(T_{sfc})\, \mathcal{T}_{\bar{\lambda}_j,sfc} + \sum_{\ell=1}^{5} \bar{B}_j(T_\ell)\, \Delta\mathcal{T}_{\bar{\lambda}_j} \quad , \qquad (14c)$$

where the constant layer thickness $\Delta\mathcal{T}_{\bar{\lambda}_j}$ is given by

$$\Delta\mathcal{T}_{\bar{\lambda}_j} = \frac{1 - \mathcal{T}_{\bar{\lambda}_j,sfc}}{5} \quad .$$

Figure 7 depicts the five layers of equal transmittance computed in the above fashion. The majority of the layers lie close to ground level where most of atmospheric contributions to upwelling thermal radiance originate. Note that the centers of the first four layers of equal transmittance lie below the center of the first equal height layer. Clearly, then, the transmittance method (14c) is the proper, most desirable coordinate system to use in order to obtain the most accurate quadrature possible for equation (13).

The satellite-observed radiance model used in this study is therefore expressed in transmission coordinates. In summary, for the continuous

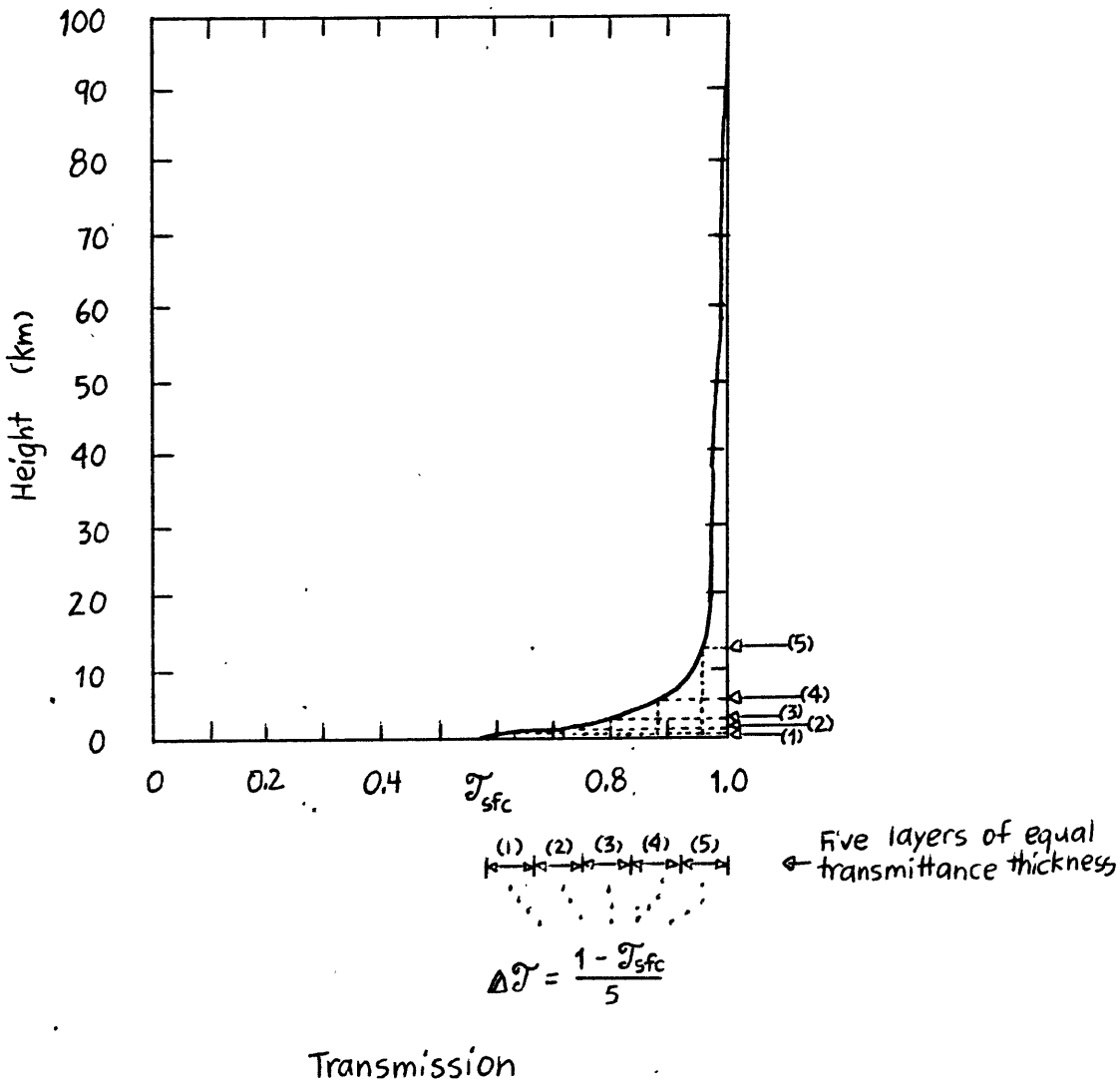

Figure 7. A Qualitative Plot of the Transmission Function as in Figure 6, But Depicting the Heights of the Centers of the Five Equal Transmittance Thickness Layers. Locations of the Centers of These Layers are Denoted by Arrows

case it is

$$I_{\bar{\lambda}}^{obs,j}(1) \cong \overline{\varepsilon_j B_j}(T_{sfc})\,\mathcal{T}_{\bar{\lambda}_j,sfc} + \int_{\mathcal{T}_{\bar{\lambda}_j,sfc}}^{1} \bar{B}_j[T(\mathcal{T}_{\bar{\lambda}_j})]\,d\mathcal{T}_{\bar{\lambda}_j} \quad . \qquad (15a)$$

In quadrature form, (15a) can be written

$$I_{\bar{\lambda}}^{obs,j}(1) \cong \overline{\varepsilon_j B_j}(T_{sfc})\,\mathcal{T}_{\bar{\lambda}_j,sfc} + \sum_{\ell=1}^{L} \bar{B}_j(T_\ell)\,\Delta\mathcal{T}_{\bar{\lambda}_j} \quad , \qquad (15b)$$

where $I_{\bar{\lambda}}^{obs,j}(1)$ is the theoretically expected satellite observed radiance, j is the NOAA-7 AVHRR channel number (j=3,4,5), $\bar{\varepsilon}_j$ is the surface emissivity valid over the spectral interval of Channel j, $\bar{B}_j(T)$ is the average value of the Planck radiance valid over the spectral interval of Channel j, $\mathcal{T}_{\bar{\lambda},j}$ is the spectral transmittance (as defined by (12a), ℓ is the layer counter, L is the number of layers to be used in the quadrature, and where each layer's thickness $\Delta\mathcal{T}_{\bar{\lambda},j}$ is given by

$$\Delta\mathcal{T}_{\bar{\lambda}_j} = \frac{1 - \mathcal{T}_{\bar{\lambda}_j,sfc}}{L} \quad . \qquad (15c)$$

Note from the above equation (15c) that the "dirtier" the window (i.e., the smaller the $\mathcal{T}_{sfc}$), the thicker the layer (the larger the $\Delta\mathcal{T}$) in altitude.

The upwelling thermal radiance measured by a satellite sensor for AVHRR Channel j is given by the equations (15). Now consider a mixed scene composed of a cloud of temperature T_{cld}, occupying a portion ρ of a sensor's field of view, along with the surface at temperature T_{sfc}, occupying the portion $\rho-1$ of the sensor field of view. Then the upwelling radiance $I_{\bar{\lambda}}^{sat,j}(\mathcal{T}=1)$ sensed by Channel j at the top of the atmosphere will be a linear combination of the integrated radiances $I_{\bar{\lambda}}^{cld,j}(1)$ (emitted by a

total cloud cover) and $I_{\bar{\lambda}}^{clr,j}(1)$ (emitted through a completely clear atmosphere), and is given by

$$I_{\bar{\lambda}}^{sat,j}(1) = (\rho-1)I_{\bar{\lambda}}^{clr,j}(1) + \rho I_{\bar{\lambda}}^{cld,j}(1), \qquad (16)$$

where ρ is the amount of cloud cover ($0<\rho<1$), and where $I_{\bar{\lambda}}^{clr,j}(1)$ and $I_{\bar{\lambda}}^{cld,j}(1)$ are computed using equations (15) with $\bar{\varepsilon}_j$, T_{sfc}, and $\mathcal{T}_{\bar{\lambda}_j,sfc}$ equated with the emissivity, temperature, and transmission for the ground and cloud top, respectively.

It is important to note that the cloud contribution $I_{\bar{\lambda}}^{cld,j}$ to the satellite-observed radiance $I_{\bar{\lambda}}^{sat,j}$ is computed assuming that clouds act as an emitting surface through which no radiation can pass. In other words, in order for (16) to be valid the optical depths τ (see equation (3)) of the clouds being sensed must be significantly greater than unity so that no radiation emitted by levels underlying the clouds passes through those clouds. The cloud transmissivity must be low (no greater, say, than 0.1). Transmissivity is defined as follows.

On the basis of conservation of energy, the following relation for the transfer of radiation through a scattering and absorbing medium must hold (Liou, 1980):

$$t_\lambda + r_\lambda + \varepsilon_\lambda = 1,$$

where t_λ is the transmissivity, r_λ is the reflectivity, and ε_λ is the emissivity. The transmissivity is defined as the ratio of the outgoing radiation to incoming radiation. Reflectivity is defined as the ratio of the reflected (backscattered) intensity to the incident intensity. Emissivity is as defined in equation (4). Note that transmissivity, reflectivity, and emissivity are each a function of wavelength, and that the range of values each can take on is in the interval [0,1].

Figures 8 and 9 contain transmissivity, emissivity, and reflectivity plots for various average cloud droplet sizes $\bar{r}$ and cloud optical depths τ, at λ=3.75 and 11.14μm, respectively. Table 3 lists the total cloud optical depths which correspond to cloud transmissivities equal to 0.1, as retrieved from the graphs in Figures 8 and 9. For a given cloud drop size $\bar{r}$, note that optical depths are generally lower in the Channel 4 and 5 spectral regions than they are in the Channel 3 spectral region. This is equivalent to stating that the attenuation (absorption plus scattering) of 3.7μm radiation by water droplet clouds is smaller than it is for radiation at 11μm.

Hence to have transmissivities that are low enough (<0.1) for the $I_{\bar{\lambda}}^{cld,j}(1)$ term of equation (16) to be adequately described by equation (15) requires that clouds within the sensor field of view have optical depths no smaller than those values listed in Table 3. This requirement restricts the successful use of equation (16) for $I_{\bar{\lambda}}^{sat,j}$ to fields of view within which only lower clouds exist. Low clouds are generally water droplet clouds; the lower they are the warmer their environment is, and hence the larger the cloud droplets will tend to be (except for ground fog, which nearly always consists of tiny water droplets). Therefore in addition to only being able to use 3.7μm Channel 3 nighttime imagery, this cloud

* * *

Droplet Size	Wavelength λ = 3.75μm	λ = 11.14μm
$\bar{r}$ = 5μm	9	2
$\bar{r}$ = 10μm	8	3
$\bar{r}$ = 20μm	7	3
$\bar{r}$ = 40μm	3	3

Table 3. List of optical depths τ where cloud transmissivities τ_λ equal 0.1, for various spherical particle sizes $\bar{r}$ and wavelengths λ

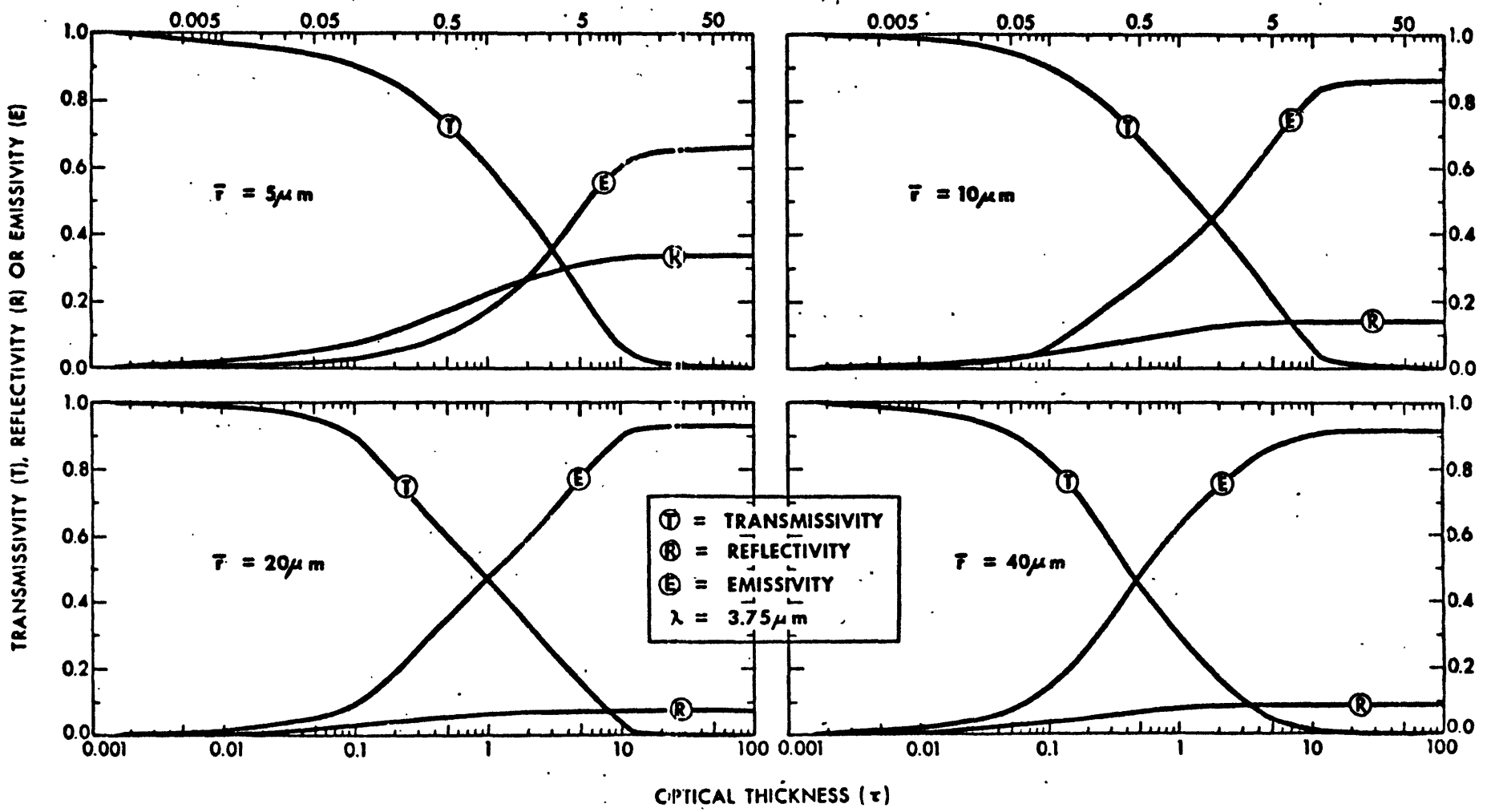

Figure 8. Transmissivity (T), Reflectivity (R), and Emissivity (E) Versus Cloud Optical Thickness (τ) for Four Different Sizes of Spherical Particles $\bar{r}$ at $\lambda = 3.75\mu m$ (after Jacobowitz and Smith, 1974)

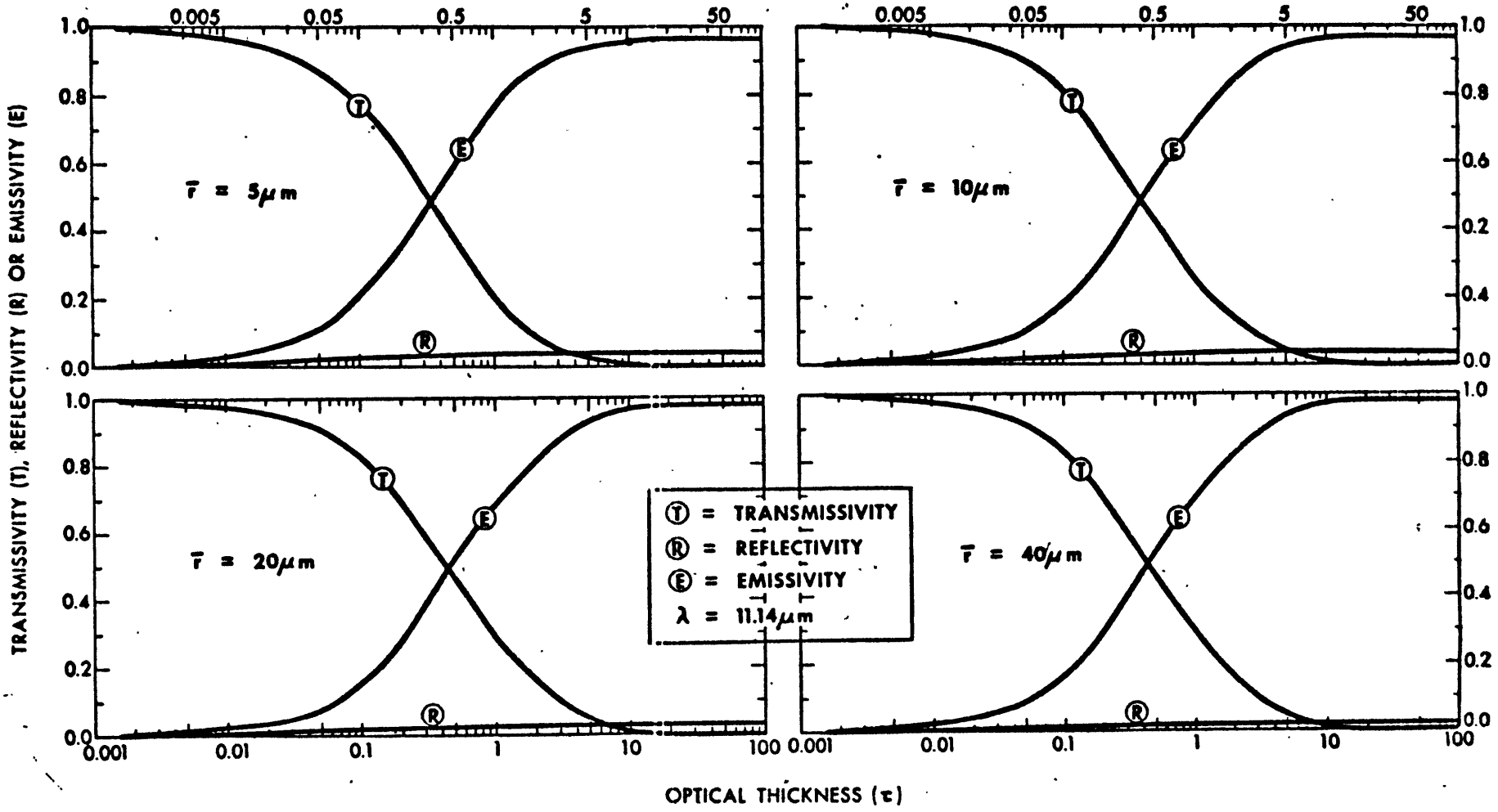

Figure 9. Transmissivity (T), Reflectivity (R), and Emissivity (E) Versus Cloud Optiacl Thickness (τ) for Four Different Sizes of Spherical Particles $\bar{r}$ at λ = 11.14μm (after Jacobowitz and Smith, 1974)

analysis study also must restrict itself to the specification of cloud parameters for lower, relatively thick water phase clouds. Higher clouds, in addition to being made up of smaller water droplets (which would subsequently require them to be of greater vertical extent to acquire the necessary optical depths), might also be composed of ice phase particles. Ice crystal attenuation properties differ significantly from those of spherical water droplets, and many types of ice clouds encountered in the atmosphere (e.g., cirrus) generally have much higher transmissivities than even the thinnest of water droplet clouds. The problem with optically thin clouds lies in the fact that significant amounts of radiation emitted from lower layers beneath the cloud pass through it and subsequently reach the satellite radiometer. A more complicated radiance model would have to be developed to account for such effects; however, keep in mind that even for high, optically thin clouds, satellite-observed brightness temperatures are typically low enough to allow for their straightforward detection.

A computer code was written to compute a series of $I_{\bar{\lambda}}^{sat,j}(1)$'s using (16) and a 15-layer model (L=15 in (15)), for a number of different atmospheres. These computations were functions of temperature profile, transmission profile (which itself is dependent on satellite seeing angle), and the amount of cloud cover ρ. A hypothetical sample set of such $I_{\bar{\lambda}}^{sat,j}(1)$ calculations for each of the NOAA-7 AVHRR Channel 3, 4, and 5 radiometers is shown in Tables 4-7.

The top part of Table 4 contains the input U.S. Standard Atmosphere transmittances $\mathcal{T}_{\bar{\lambda},j}$ for each of the three AVHRR channels indicated, along with the input temperature profile. The transmittances were calculated using AFGL's computer code RSAT (personal communication, Dr. Robert A.

LEVEL (STD)	HEIGHT (KM)	TEMPERATURE (DEG K)	TRANSMITTANCE CH 3	CH 4	CH 5
16	70	219.7	.99999	.99999	.99999
15	50	270.6	.99998	.99997	.99996
14	25	221.6	.99953	.99993	.99995
13	20	216.6	.99885	.99985	.99990
12	15	216.6	.99715	.99965	.99980
11	10	223.2	.99272	.99907	.99950
10	9	229.7	.99119	.99879	.99927
9	8	236.2	.98917	.99828	.99871
8	7	242.7	.98642	.99737	.99747
7	6	249.2	.98266	.99576	.99502
6	5	255.7	.97737	.99288	.99026
5	4	262.2	.96973	.98770	.98124
4	3	268.7	.95859	.97824	.96453
3	2	275.1	.94253	.96093	.93470
2	1	281.6	.92056	.93099	.88591
1	0	288.1	.89220	.88348	.81318

SFC EMISSIVITY CH3	CH4	CH5	CLD EMISSIVITY CH3	CH4	CH5
.93	.97	.97	.90	.96	.96

	CHANNEL 3					CHANNEL 4					CHANNEL 5			
LEVEL (NONSTD)	HEIGHT (KM)	TEMP (DEG K)	PRES (MB)	TRANS	LEVEL (NONSTD)	HEIGHT (KM)	TEMP (DEG K)	PRES (MB)	TRANS	LEVEL (NONSTD)	HEIGHT (KM)	TEMP (DEG K)	PRES (MB)	TRANS
16	70.00	220.0	.1	.99999	16	70.00	220.0	.1	.99999	16	70.00	220.0	.1	.99999
15	10.09	223.1	262.1	.99280	15	4.87	256.5	550.2	.99222	15	4.70	257.7	563.5	.98754
14	6.79	244.1	424.1	.98562	14	3.66	264.4	645.6	.98446	14	3.63	264.6	647.8	.97508
13	5.20	254.4	526.8	.97843	13	2.91	269.3	709.6	.97669	13	2.94	269.1	707.2	.96263
12	4.20	260.9	601.5	.97125	12	2.46	272.1	751.7	.96892	12	2.52	271.8	746.3	.95017
11	3.49	265.5	659.7	.96406	11	2.01	275.0	793.8	.96115	11	2.10	274.5	785.5	.93772
10	2.89	269.4	711.2	.95687	10	1.75	276.7	821.1	.95339	10	1.81	276.4	815.0	.92527
9	2.45	272.2	753.2	.94969	9	1.49	278.4	848.0	.94562	9	1.55	278.0	841.5	.91281
8	2.00	275.1	795.1	.94250	8	1.23	280.1	874.9	.93785	8	1.30	279.7	867.9	.90036
7	1.67	277.2	829.0	.93532	7	.98	281.7	900.8	.93008	7	1.04	281.3	894.4	.88790
6	1.34	279.4	862.9	.92813	6	.82	282.8	919.5	.92232	6	.86	282.5	915.1	.87545
5	1.02	281.5	896.8	.92094	5	.65	283.8	938.2	.91455	5	.68	283.6	934.6	.86300
4	.76	283.2	926.0	.91376	4	.49	284.9	956.9	.90678	4	.51	284.8	954.2	.85054
3	.51	284.8	955.0	.90657	3	.33	286.0	975.6	.89901	3	.34	285.9	973.8	.83809
2	.25	286.5	984.0	.89939	2	.16	287.0	994.3	.89125	2	.17	287.0	993.4	.82563
1	.00	288.1	1013.0	.89220	1	.00	288.1	1013.0	.88348	1	.00	288.1	1013.0	.81318

Table 4. The Input U.S. Standard Atmosphere Transmission and Temperature Profile (Top), Ground and Cloud Emissivities (Middle), and the Vertical Grid Levels for the 15 Layer Equal Transmittance Radiance Model Calculations (Bottom)

McClatchey). This code is designed to compute atmospheric spectral transmittance functions (as defined by equation (12a)), and takes into account absorption by well-mixed gases, water vapor, the effects of varying atmospheric temperature, and the effect of varying satellite viewing angle (which determines optical path length). Tables of the spectral transmittance functions for each of the AVHRR window Channels 3, 4, and 5 are listed in Appendix A as a function of atmosphere (e.g., Arctic, U.S. Standard, and Tropical) and satellite viewing angle.

In the middle of Table 4 are listed the cloud and surface emissivities that went into the 15-layer radiative transfer model. A list of emissivities as a function of wavelength for the clouds and surfaces encountered in this study can be found in Appendix B.

Finally, at the bottom of Table 4 are listed the levels bounding the 15 layers of equal transmittance thickness, along with their corresponding temperatures, for each of the AVHRR Channels 3, 4, and 5. Observe that nearly all the layers of the transmittance coordinate grid lie in the lowest 5 km or so of the atmosphere (recall the previous arguments leading up to Figure 7), as is well illustrated in Figure 10. The transmittances listed in Table 4 were computed for U.S. Standard atmospheric temperature and aerosol profiles, and also for a vertical path from the ground to space (i.e., the satellite viewing angle is zero). Note that the $\Delta \mathcal{T}_{\bar{\lambda}}$ for Channel 5 is the largest of all three channels; this is due to the fact that Channel 5 is the dirtiest of the 3 infrared AVHRR windows. With surface/cloud emissivities and atmospheric transmittances and temperatures entered in, the radiance code then computes estimates of satellite-measured upwelling thermal radiances as defined by equation (16).

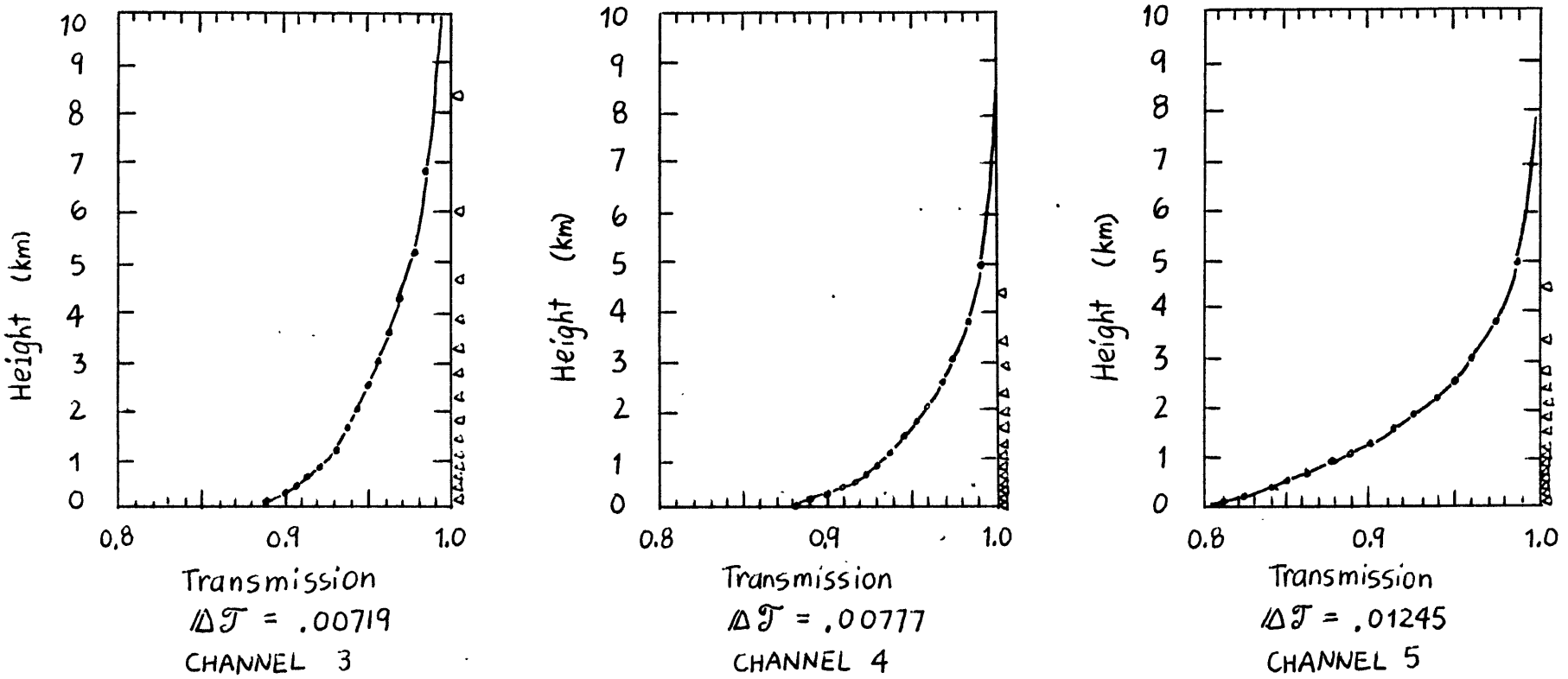

Figure 10. Plots of Transmittance for Each of the NOAA-7 AVHRR Channels as a Function of Altitude for the U.S. Standard Atmosphere Example of Table 4. The Arrowheads at the Right Side of Each of the Three Plots Indicate the Position of the Centers of Layers of Equal Transmittance Thickness

Tables 5a and 5b list the results of Channel 3 radiance computations $I_{\bar{\lambda}}^{sat,j}(1)$ for the temperature, transmittance profile of Table 4 and Figure 10, and for various cloud top heights and fractional cloud covers. Fractional cloud cover runs along the top of each Table, and varies from 0 (clear) to 10/10's (completely cloudy) coverage in steps of 1/10. Along the side of each of the Tables is listed the height and temperature of the cloud top (in km and ^{o}K, respectively), just next to a list of pressures which correspond to the indicated heights and temperatures. (The pressures are just reasonable estimates of actual case pressure values, and are listed for reference purposes only.) To find the upwelling thermal radiance measured by the Channel 3 sensor whose field of view contains a cloud covering 80% of the underlying ground, and whose top temperature is 277.2 ^{o}K, slide across the top of Table 5a to the 8/10 column and down the Table to the 277.2 ^{o}K (1.67 km) row to read off a thermal radiance value of .169036 Watts m^{-2} μm^{-1} $ster^{-1}$. A simple linear interpolation can be used to determine thermal radiance values for clouds whose fractional coverage and/or top temperatures lie between the values listed in the Tables.

Tables 5a and 5b contain essentially the same information; they differ only in the atmospheric vertical extent of their tabulations (note the differences in the heights of the cloud top levels listed down the left side of the Tables). Table 5a contains radiances for cloud tops at each of the lowest 15 levels which bound the layers of equal transmittance thickness, while Table 5b lists radiances for cloud tops at the lowest 10 km of the atmosphere in increments of 1 km. Table 5b was derived from Table 5a using a simple linear interpolation scheme.

Tables 6 and 7 contain analogous radiance calculations to those in

SATELLITE-OBSERVED THERMAL RADIANCE FOR NOAA-7 AVHRR CHANNEL 3, IN WATTS/M2-MICRON-STER

CLOUD HGT (KM)	USTD PRES (MB)	TEMP (DEG K)	TOTAL CLOUD COVERAGE (TENTHS OF GROUND COVERED) 0/10	1/10	2/10	3/10	4/10	5/10	6/10	7/10	8/10	9/10	10/10
10.09	262.1	223.1	.251665	.227054	.202444	.177833	.153223	.128613	.104002	.079392	.054781	.030171	.005560
6.79	424.1	244.1	.251665	.228869	.206074	.183279	.160483	.137688	.114892	.092097	.069301	.046506	.023710
5.20	526.8	254.4	.251665	.230936	.210207	.189478	.168749	.148020	.127291	.106562	.085833	.065104	.044375
4.20	601.5	260.9	.251665	.232920	.214175	.195430	.176685	.157940	.139196	.120451	.101706	.082961	.064216
3.49	659.7	265.5	.251665	.234737	.217809	.200881	.183953	.167025	.150097	.133169	.116242	.099314	.082386
2.89	711.2	269.4	.251665	.236588	.221511	.206434	.191357	.176280	.161203	.146126	.131049	.115972	.100895
2.45	753.2	272.2	.251665	.238169	.224674	.211179	.197684	.184188	.170693	.157198	.143702	.130207	.116712
2.00	795.1	275.1	.251665	.239880	.228095	.216311	.204526	.192741	.180957	.169172	.157387	.145602	.133818
1.67	829.0	277.2	.251665	.241336	.231008	.220679	.210351	.200022	.189693	.179365	.169036	.158708	.148379
1.34	862.9	279.4	.251665	.242917	.234170	.225423	.216675	.207928	.199180	.190433	.181686	.172938	.164191
1.02	896.8	281.5	.251665	.244632	.237599	.230566	.223533	.216500	.209468	.202435	.195402	.188369	.181336
.76	926.0	283.2	.251665	.246081	.240498	.234914	.229331	.223747	.218164	.212580	.206997	.201413	.195830
.51	955.0	284.8	.251665	.247597	.243528	.239460	.235392	.231324	.227255	.223187	.219119	.215051	.210982
.25	984.0	286.5	.251665	.249202	.246739	.244276	.241814	.239351	.236888	.234425	.231962	.229500	.227037
.00	1013.0	288.1	.251665	.251665	.251665	.251665	.251665	.251665	.251665	.251665	.251665	.251665	.251665

Table 5a. Channel 3 Radiance Computations for Various Fractional Cloud Covers and Cloud Top Heights. The Heights are the Levels Bounding the Lowest 15 Equal-Transmittance Layers

SATELLITE-OBSERVED THERMAL RADIANCE FOR NOAA-7 AVHRR CHANNEL 3, IN WATTS/M2-MICRON-STER

CLOUD HGT (KM)	USTD PRES (MB)	TEMP (DEG K)	TOTAL CLOUD COVERAGE (TENTHS OF GROUND COVERED) 0/10	1/10	2/10	3/10	4/10	5/10	6/10	7/10	8/10	9/10	10/10
10	265.0	223.2	.251665	.227106	.202548	.177990	.153431	.128873	.104315	.079756	.055198	.030640	.006081
9	308.0	229.7	.251665	.227655	.203645	.179636	.155626	.131616	.107607	.083597	.059587	.035578	.011568
8	356.5	236.2	.251665	.228204	.204743	.181282	.157821	.134360	.110899	.087438	.063977	.040516	.017055
7	411.1	242.7	.251665	.228752	.205840	.182928	.160015	.137103	.114191	.091278	.068366	.045453	.022541
6	472.2	249.2	.251665	.229895	.208124	.186354	.164584	.142814	.121043	.099273	.077503	.055733	.033962
5	540.5	255.7	.251665	.231333	.211002	.190670	.170339	.150007	.129676	.109344	.089013	.068681	.048349
4	616.6	262.2	.251665	.233430	.215194	.196959	.178724	.160489	.142254	.124018	.105783	.087548	.069313
3	701.2	268.7	.251665	.236257	.220849	.205441	.190034	.174626	.159218	.143810	.128403	.112995	.097587
2	795.0	275.1	.251665	.239875	.228086	.216296	.204506	.192717	.180927	.169138	.157348	.145558	.133769
1	898.6	281.6	.251665	.244730	.237796	.230861	.223927	.216992	.210058	.203123	.196189	.189255	.182320
0	1013.0	288.1	.251665	.251665	.251665	.251665	.251665	.251665	.251665	.251665	.251665	.251665	.251665

Table 5b. Channel 3 Radiance Computations for Various Fractional Cloud Covers and Cloud Top Heights. The Heights Range From 0 to 10 km in Increments of 1 km

SATELLITE-OBSERVED THERMAL RADIANCE FOR NOAA-7 AVHRR CHANNEL 4, IN WATTS/M2-MICRON-STER

CLOUD HGT (KM)	USTD PRES (MB)	TEMP (DEG K)	TOTAL CLOUD COVERAGE (TENTHS OF GROUND COVERED) 0/10	1/10	2/10	3/10	4/10	5/10	6/10	7/10	8/10	9/10	10/10
4.87	550.2	256.5	7.655153	7.323159	6.991164	6.659170	6.327176	5.995182	5.663187	5.331193	4.999198	4.667204	4.335210
3.66	645.6	264.4	7.655153	7.395975	7.136797	6.877619	6.618441	6.359263	6.100084	5.840907	5.581729	5.322551	5.063373
2.91	709.6	269.3	7.655153	7.443793	7.232434	7.021074	6.809714	6.598355	6.386995	6.175635	5.964275	5.752916	5.541556
2.46	751.7	272.1	7.655153	7.473246	7.291338	7.109430	6.927523	6.745615	6.563707	6.381800	6.199892	6.017984	5.836077
2.01	793.8	275.0	7.655153	7.503428	7.351703	7.199977	7.048251	6.896526	6.744801	6.593075	6.441349	6.289624	6.137898
1.75	821.1	276.7	7.655153	7.521884	7.388615	7.255344	7.122075	6.988807	6.855536	6.722267	6.588998	6.455729	6.322459
1.49	848.0	278.4	7.655153	7.540160	7.425168	7.310175	7.195182	7.080190	6.965197	6.850204	6.735210	6.620218	6.505225
1.23	874.9	280.1	7.655153	7.558609	7.462065	7.365520	7.268976	7.172432	7.075888	6.979343	6.882799	6.786255	6.689711
.98	900.8	281.7	7.655153	7.576425	7.497696	7.418967	7.340239	7.261510	7.182781	7.104053	7.025324	6.946595	6.867867
.82	919.5	282.8	7.655153	7.588297	7.521441	7.454585	7.387729	7.320873	7.254017	7.187160	7.120304	7.053449	6.986592
.65	938.2	283.8	7.655153	7.600201	7.545249	7.490296	7.435345	7.380393	7.325440	7.270489	7.215536	7.160584	7.105633
.49	956.9	284.9	7.655153	7.612126	7.569099	7.526073	7.483046	7.440019	7.396992	7.353965	7.310938	7.267911	7.224884
.33	975.6	286.0	7.655153	7.624083	7.593013	7.561943	7.530873	7.499804	7.468733	7.437663	7.406592	7.375523	7.344453
.16	994.3	287.0	7.655153	7.636059	7.616964	7.597870	7.578775	7.559681	7.540586	7.521492	7.502398	7.483303	7.464209
.00	1013.0	288.1	7.655153	7.655153	7.655153	7.655153	7.655153	7.655153	7.655153	7.655153	7.655153	7.655153	7.655153

Table 6a. Channel 4 Radiance Computations for Various Fractional Cloud Covers and Cloud Top Heights. The Heights are the Levels Bounding the Lowest 15 Equal-Transmittance Layers

SATELLITE-OBSERVED THERMAL RADIANCE FOR NOAA-7 AVHRR CHANNEL 4, IN WATTS/M2-MICRON-STER

CLOUD HGT (KM)	USTD PRES (MB)	TEMP (DEG K)	TOTAL CLOUD COVERAGE (TENTHS OF GROUND COVERED) 0/10	1/10	2/10	3/10	4/10	5/10	6/10	7/10	8/10	9/10	10/10
10	265.0	223.2	7.655153	7.303428	6.951701	6.599976	6.248250	5.896524	5.544798	5.193072	4.841346	4.489620	4.137895
9	308.0	229.7	7.655153	7.307276	6.959399	6.611522	6.263644	5.915768	5.567890	5.220013	4.872135	4.524259	4.176381
8	356.5	236.2	7.655153	7.311125	6.967096	6.623067	6.279038	5.935011	5.590981	5.246953	4.902925	4.558896	4.214868
7	411.1	242.7	7.655153	7.314973	6.974793	6.634613	6.294434	5.954254	5.614074	5.273893	4.933714	4.593534	4.253354
6	472.2	249.2	7.655153	7.318822	6.982491	6.646159	6.309828	5.973497	5.637165	5.300835	4.964503	4.628172	4.291841
5	540.5	255.7	7.655153	7.322671	6.990188	6.657705	6.325223	5.992741	5.660257	5.327775	4.995292	4.662809	4.330327
4	616.6	262.2	7.655153	7.375438	7.095721	6.816006	6.536290	6.256575	5.976858	5.697143	5.417426	5.137711	4.857995
3	701.2	268.7	7.655153	7.438051	7.220949	7.003847	6.786746	6.569644	6.352542	6.135440	5.918338	5.701237	5.484135
2	795.0	275.1	7.655153	7.504326	7.353499	7.202672	7.051845	6.901018	6.750191	6.599364	6.448537	6.297709	6.146883
1	898.6	281.6	7.655153	7.575055	7.494958	7.414861	7.334764	7.254666	7.174568	7.094471	7.014373	6.934276	6.854178
0	1013.0	288.1	7.655153	7.655153	7.655153	7.655153	7.655153	7.655153	7.655153	7.655153	7.655153	7.655153	7.655153

Table 6b. Channel 4 Radiance Computations for Various Fractional Cloud Covers and Cloud Top Heights. The Heights Range From 0 to 10 km in Increments of 1 km

SATELLITE-OBSERVED THERMAL RADIANCE FOR NOAA-7 AVHRR CHANNEL 5, IN WATTS/M2-MICRON-STER

CLOUD HGT (KM)	USTD PRES (MB)	TEMP (DEG K)	TOTAL CLOUD COVERAGE (TENTHS OF GROUND COVERED) 0/10	1/10	2/10	3/10	4/10	5/10	6/10	7/10	8/10	9/10	10/10
4.70	563.5	257.7	7.200602	6.922214	6.643826	6.365439	6.087051	5.808664	5.530276	5.251888	4.973501	4.695114	4.416726
3.63	647.8	264.6	7.200602	6.979959	6.759317	6.538675	6.318033	6.097391	5.876749	5.656107	5.435465	5.214823	4.994181
2.94	707.2	269.1	7.200602	7.019393	6.838184	6.656977	6.475768	6.294560	6.113351	5.932143	5.750936	5.569727	5.388518
2.52	746.3	271.8	7.200602	7.043383	6.886165	6.728947	6.571728	6.414510	6.257291	6.100072	5.942854	5.785636	5.628417
2.10	785.5	274.5	7.200602	7.067671	6.934740	6.801810	6.668880	6.535950	6.403018	6.270088	6.137158	6.004228	5.871297
1.81	815.0	276.4	7.200602	7.085364	6.970127	6.854891	6.739655	6.624417	6.509180	6.393943	6.278707	6.163470	6.048233
1.55	841.5	278.0	7.200602	7.100743	7.000885	6.901028	6.801169	6.701312	6.601453	6.501595	6.401737	6.301880	6.202022
1.30	867.9	279.7	7.200602	7.116150	7.031698	6.947248	6.862797	6.778345	6.693893	6.609442	6.524991	6.440540	6.356089
1.04	894.4	281.3	7.200602	7.131575	7.062548	6.993522	6.924495	6.855469	6.786441	6.717415	6.648388	6.579362	6.510335
.86	915.1	282.5	7.200602	7.142817	7.085033	7.027250	6.969467	6.911683	6.853899	6.796115	6.738332	6.680549	6.622765
.68	934.6	283.6	7.200602	7.153230	7.105859	7.058488	7.011117	6.963746	6.916374	6.869002	6.821632	6.774261	6.726890
.51	954.2	284.8	7.200602	7.163595	7.126590	7.089584	7.052579	7.015574	6.978567	6.941562	6.904556	6.867551	6.830545
.34	973.8	285.9	7.200602	7.173914	7.147226	7.120540	7.093852	7.067165	7.040477	7.013790	6.987103	6.960416	6.933728
.17	993.4	287.0	7.200602	7.184183	7.167766	7.151348	7.134931	7.118513	7.102095	7.085676	7.069260	7.052841	7.036424
.00	1013.0	288.1	7.200602	7.200602	7.200602	7.200602	7.200602	7.200602	7.200602	7.200602	7.200602	7.200602	7.200602

Table 7a. Channel 5 Radiance Computations for Various Fractional Cloud Covers and Cloud Top Heights. The Heights are the Levels Bounding the Lowest 15 Equal-Transmittance Layers

SATELLITE-OBSERVED THERMAL RADIANCE FOR NOAA-7 AVHRR CHANNEL 5, IN WATTS/M2-MICRON-STER

CLOUD HGT (KM)	USTD PRES (MB)	TEMP (DEG K)	TOTAL CLOUD COVERAGE (TENTHS OF GROUND COVERED) 0/10	1/10	2/10	3/10	4/10	5/10	6/10	7/10	8/10	9/10	10/10
10	265.0	223.2	7.200602	6.902390	6.604178	6.305967	6.007755	5.709544	5.411332	5.113120	4.814909	4.516698	4.218486
9	308.0	229.7	7.200602	6.906129	6.611656	6.317183	6.022711	5.728239	5.433765	5.139293	4.844821	4.550348	4.255876
8	356.5	236.2	7.200602	6.909867	6.619131	6.328401	6.037667	5.746934	5.456200	5.165465	4.874733	4.583999	4.293265
7	411.1	242.7	7.200602	6.913607	6.626612	6.339618	6.052623	5.765629	5.478633	5.191639	4.904645	4.617650	4.330655
6	472.2	249.2	7.200602	6.917346	6.634089	6.350835	6.067579	5.784324	5.501067	5.217812	4.934556	4.651300	4.368045
5	540.5	255.7	7.200602	6.921084	6.641568	6.362052	6.082535	5.803019	5.523501	5.243985	4.964469	4.684952	4.405436
4	616.6	262.2	7.200602	6.960006	6.719411	6.478816	6.238220	5.997625	5.757030	5.516434	5.275839	5.035244	4.794648
3	701.1	268.7	7.200602	7.015776	6.830951	6.646127	6.461301	6.276476	6.091650	5.906825	5.722001	5.537175	5.352350
2	794.0	275.1	7.200602	7.073751	6.946901	6.820052	6.693202	6.566352	6.439502	6.312652	6.185802	6.058952	5.932102
1	898.6	281.6	7.200602	7.134061	7.067525	7.000987	6.934448	6.867910	6.801372	6.734833	6.668295	6.601757	6.535218
0	1013.0	288.1	7.200602	7.200602	7.200602	7.200602	7.200602	7.200602	7.200602	7.200602	7.200602	7.200602	7.200602

Table 7b. Channel 5 Radiance Computations for Various Fractional Cloud Covers and Cloud Top Heights. The Heights Range From 0 to 10 km in Increments of 1 km

Table 5, but for Channels 4 and 5, respectively.

Now consider the spectral transmittance and temperature profiles for a particular scene and for each of the 3 AVHRR channels, along with a set of actual satellite-observed radiances for each channel. It is possible to use these measured radiances in conjunction with tables of theoretically computed radiances similar to Tables 5-7 to infer cloud amount and cloud top height for a particular scene by intercomparing the measured radiance values against the tabulated ones. Two independent observations of radiance are necessary in order to be able to uniquely determine the two unknown parameters cloud amount and cloud top height. Nighttime radiance measurements from any two of the three AVHRR Channels 3, 4, and 5 would serve as independent measurements, while the third can be used as a check. However, in this study it was quickly discovered that each of the three channels' radiance measurements are needed to specify cloud amount and cloud top height, since in general the functional dependence of satellite observed radiances on fractional cloud cover and cloud top altitude was found not to vary significantly enough among channels to work with only two independent measurements. The dependence of $I_{\bar{\lambda}}^{sat,j}(0)$ (equation (16)) on cloud top altitude z and cloud amount ρ is strongly similar among channels because the $I_{\bar{\lambda}}^{sat,j}$ as a function of channel number j are not strictly independent measurements. In other words since each of the AVHRR Channels 3, 4, and 5 are windows, then given one radiance measurement ($I_{\bar{\lambda}}^{sat,4}(0)$, say), then the Channels 3 and 5 radiance measurements ($I_{\bar{\lambda}}^{sat,3}(0)$ and $I_{\bar{\lambda}}^{sat,5}(0)$, respectively) can be mathematically predicted to nearly within measurement error as some linear function of the Channel 4 radiance.

An example follows of how the multispectral cloud analysis tech-

nique is applied. Consider the emissivities and temperature/transmission profiles listed in Table 4 and the subsequent computations of satellite observed radiances in Tables 5-7 (as defined by (16)) as being representative of a hypothetical cloud scene. Suppose in addition that the satellite measured radiances for Channels 3, 4, and 5 are .134, 6.379, and 6.028 Watts m^{-2} μm^{-1} $ster^{-1}$, respectively. When comparing each of these three radiances with the appropriate Tables 5-7, the following plots of cloud height (every .5 km) versus cloud cover (every .05 of sky covered) are obtained.

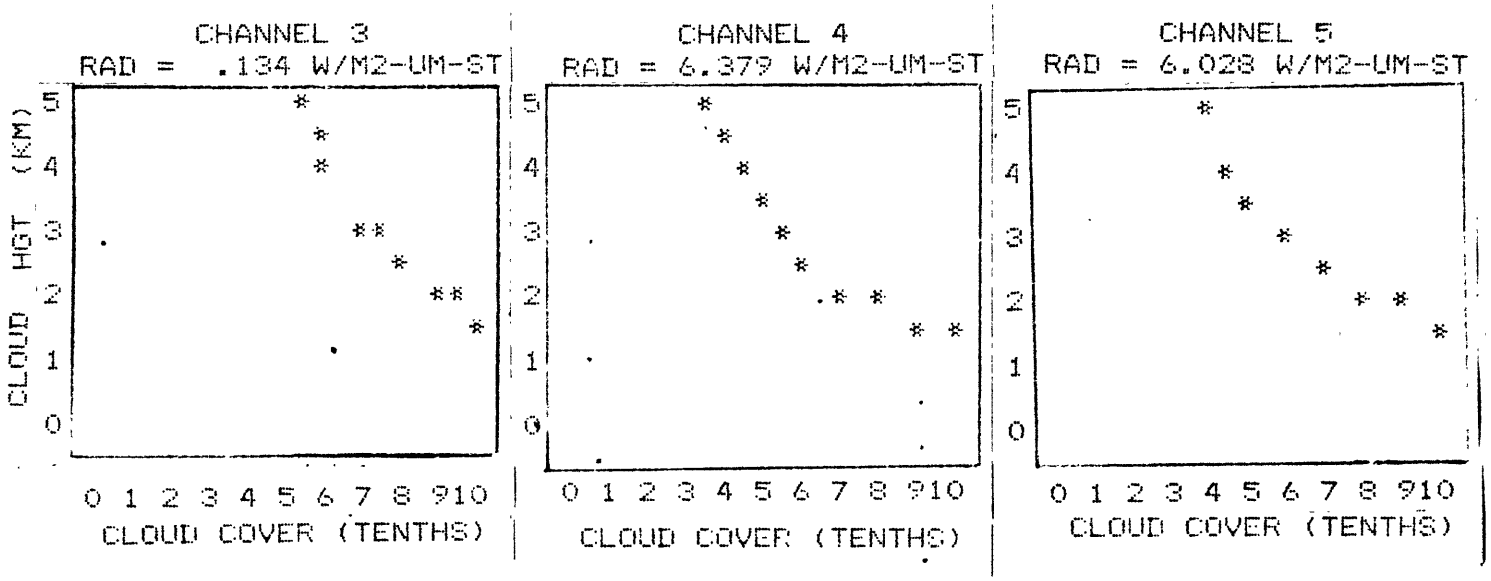

These plots contain all the theoretically possible paired values of cloud cover and cloud top height, as obtained through the use of Tables 5, 6, and 7, that correspond to the aforementioned hypothetical satellite radiances. Note, as previously mentioned, that one single radiance measurement could be the result of a number of vastly different cloud amounts and cloud top heights. Note too the general shape of the cloud top height/cloud amount curves is quite similar for each of the three channels, as should be expected. The above curves show the dependence of a given satellite observed radiance on cloud amount and top altitude to be

such that as cloud cover (more precisely, earth cover) increases, cloud top altitude decreases.

Once each of these three curves are generated, they are then overlayed on top of each other to determine where the respective curves intersect. The intersection of these curves is then the cloud amount, cloud top height pair which is valid for the simultaneous radiances. The following plot illustrates the result of such an exercise.

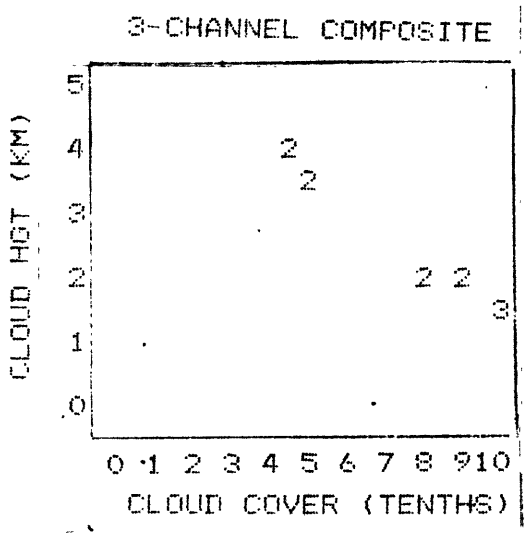

Only those points where an intersection of two or more curves occur are plotted. The number "2" indicates that two of the three radiance cloud amount versus cloud top height curves pass through that point, while the number "3" indicates all three curves pass through that point. The spot where the highest number of intersections occurs reveals the cloud amount and cloud top height for the given set of simultaneously observed radiances. Thus, for this example, the 3-channel composite plot of cloud cover versus cloud top height indicates the aforementioned radiances were measured in a field of view containing 100% coverage (10/10) of clouds whose tops are at 1.5 km.

It is most certainly not always guaranteed that the intersection of

three independent radiance curves will yield a clearly decisive cloud amount/top height decision. In fact, it is anticipated that there will be instances where large clusters of intersections exist, with differences of only a few tenths of coverage or a few hundred meters in cloud top altitude among the intersection points. Such results make the choice of cloud cover and cloud top altitudes ambiguous. Sensible decision rules can then be employed (which preserve continuity of cloud analysis from pixel to pixel or which choose the graphical centers of said clusters as the analysis result) for those instances where there is no clear-cut, definitive determination of the unknown cloud parameters on the part of the algorithm. Another way to alleviate this problem would be to reconstruct the cloud amount/cloud top altitude curves using a more fine amount/altitude resolution (e.g., for every .025 sky cover and/or every .25 km, instead of every .05 sky cover and every .5 km), thus increasing the likelihood that the curves will intersect in a more decisive fashion.

The algorithm results of some sample imagery case tests are discussed in the next section.

III. Tests and Results

A. The Cloud Analysis Procedure

The development of an automated cloud analysis routine requires a sample set of cloud truth AVHRR imagery cases. The AVHRR data saves used for this study were acquired on tape from NOAA NESDIS (National Environmental, Satellite, and Data Information Service), and are mainly from 11 June 1982 NOAA-7 half-orbits which collectively cover nearly all of the northern hemisphere and span a period of roughly 7 hours. Such a large data set is more than adequate for this study and allows for a good di-

versity of cloud samples for both this and any future cloud studies involving NOAA-7 AVHRR imagery classification techniques.

The NOAA-7 polar orbiter data obtained on tape is raw data that has been quality controlled, grouped together into discrete sets, and to which earth location and grayshade calibration information has been added. The AVHRR data is available from NOAA NESDIS in three different formats, as described in the following paragraphs.

Direct transmission to earth of AVHRR data in real time is called High Resolution Picture Transmission (HRPT) data, and has a nominal 1 km resolution at satellite nadir. There are 2048 elements per channel in an HRPT scan line, or 10240 samples per AVHRR scan. Each sample has 10-bit accuracy. The satellite does not possess enough onboard storage capabilities to store very much 1 km data at a time; however, about 10 minutes of data per orbit can be selectively stored on the onboard tape recorders and read out at a later time when the satellite conveniently passes within range of a ground receiver station. When HRPT data is stored and read out in this fashion, it is called Local Area Coverage (LAC) data. LAC data may be recorded over any portion of the world (Kidwell, 1983).

The full resolution real time AVHRR data is also sampled and processed onboard the satellite into Global Area Coverage (GAC) data. Four out of every five samples along the scanline are used to compute one average value, and the data from only every third line is processed. Consequently, the spatial resolution of GAC data at subpoint is 4.0km × 3.3km, but is generally treated as having nominal 4 km resolution. All of the GAC data computed during a satellite pass is stored onboard and transmitted to earth on command. The 10-bit accuracy of the

AVHRR HRPT data is retained throughout this process (Kidwell, 1983).

In the imagery sample selection procedure, simultaneous nighttime Channel 3, 4, and 5 GAC imagery were first displayed on AFGL's Man-computer Interactive Data Access System (McIDAS). The imagery was then examined to find potential cases on which to test the multispectral analysis technique described in the previous sections. Next, McIDAS's interactive cursor was positioned over the AVHRR imagery of interest. A McIDAS interactive image display routine, written for this study, was then invoked to transfer from disk to tape the colocated Channel 3, 4, and 5 digital data corresponding to the satellite imagery underneath the 4 × 4 square cursor. A 4 × 4 sample array of GAC data nominally corresponds to a 16km × 16km area on the Earth's surface. In addition to the 48 AVHRR 10-bit grayshades (4 × 4 pixels for each of the 3 channels), bookkeeping information such as sensor scan element numbers, data times, earth location, and data calibration coefficients for each datum were automatically saved. Each of the samples used for testing was first examined by fellow scientists at AFGL for purposes of a subjective analysis cloud truth. After visual inspection of the data, care was taken to save only nighttime imagery samples within which only one type of lower level cloud was believed to exist. Nearby surface weather reports and upper air observations were also available for each of the interactively chosen samples. Table 8 lists the final four imagery samples selected for testing by this study. They were selected for their well-defined cloud features, and for their proximity to nearby surface and upper air stations. Reports from these stations were used as input to the theoretical computations of satellie-observed radiances, in a manner exactly analogous to that described in Part II, Section E.

Sample Label	Earth Location	Background (for emissivity considerations)	Characteristic Features of the Sample (subjectively determined)
A	43.8 N, 99.4 W	The Dakota hills, small rivers	Sharp cloud edge
B	51.0 N, 94.4 W	Forests, lakes of south central Canada	Well-defined cloud band
C	33.4 N, 80.4 W	Lowland marshes, vegetation	Sharp fog edge
D	40.6 N, 75.1 W	Trees, small cities	Generally broken to overcast conditions

Table 8. Characteristics of the Four AVHRR Imagery Samples Used to Test the Multispectral Cloud Analysis Technique

B. Results

The results of the multispectral cloud parameter retrieval method discussed in Part II are described in the following paragraphs for each of the samples A-D listed in Table 8.

The radiance computation program was written on the AFGL GOULD 32-bit general purpose batch processor. The radiance calculation code which computes the $I_{\bar{\lambda}}^{sat,j}$ as given by (16) is initialized interactively in the following manner. First, the proper transmission functions as determined by Earth location and satellite local scene zenith angle are entered into the program by the user for the image sample to be processed (see Appendix A). Next is keyed in an atmospheric temperature profile valid for the image sample time and location, using a nearby RAOB. Surface temperatures T_{sfc}, whose specification is very important to the accuracy of the theoretically computed window radiances and subsequently to to the success of the cloud analysis technique as a whole, are determined using attenuation-corrected clear column Channel 4 brightness temperatures T_{Br}, or by using nearby nighttime surface weather station temperature observations. The former method is usually preferred since quite often observations of ambient air temperatures are not characteristic of underlying surface skin temperatures; even at night. The bulk of an observed satellite radiance is highly sensitive to the value of T_{sfc}, so that care must be taken in specifying it.

Finally, surface and cloud emissivities valid for each of the AVHRR Channels 3, 4, and 5 are entered into the program (see Appendix B for a discussion of emmissivity), along with the simultaneously observed radiances for each of the 16 pixels of the 4 × 4 AVHRR image sample. The surface emissivities were determined for each sample through trial selec-

tion procedures. Using the Tables in Appendix B, first-guess emissivities were entered into the radiance program. The radiances thus obtained were then compared to imagery clear-column radiances observed near the sample imagery. If the computed clear-column radiances did not match up with the observed clear-column radiances, adjustments to the surface emissivities were made (by trial and error) until they did. Finally, when the observed and computed clear radiances matched, the particular emissivity used for that calculation was used for the nearby cloud imagery sample. Cloud emissivities were selected using the Tables in Appendix B, along with an inter-channel comparison of the differences in the cloudy pixel satellite-observed brightness temperatures. The program proceeds to compute radiances such as those listed in Tables 5-7, and then continues on to generate cloud cover versus cloud top altitude plots similar to those shown at the end of Part II, Section E. Subsequent cloud analysis results are then checked for accuracy using nearby surface weather station observations of cloud amount and cloud base height, in addition to the subjective analysis of the sample imagery. For each of the samples A-D listed in Table 8, Table 9 lists the values of the surface and cloud emissivities, surface skin temperatures, and upper air RAOB stations whose soundings were used to initialize the radiance calculation model.

Sample A

The imagery of Sample A shows a well-defined cloud edge, with the majority of the clouds pretty much filling the right half of the 4 × 4 pixel array. The corresponding satellite observed Channels 3, 4, and 5 brightness temperatures T_{Br} (see equation (8)), plotted in Figure 11a, confirm this analysis. It should be pointed out here that these brightness temperatures are direct observations based on satellite measured

Sample/Feature	Emissivities						Skin Temperature	Nearby Sfc Stns	Nearby RAOB Stns
	Surface			Cloud					
	Ch3	Ch4	Ch5	Ch3	Ch4	Ch5	T_{sfc}		
A, Cloud Edge	.85	.96	.96	.82	.96	.96	286.0 °K	MHE FSD YKN	72654 Huron, SD
B, Cloud Band	.84	.96	.96	.82	.96	.96	280.9 °K	YQK	72747 Int'nl. Falls, MN
C, Fog Edge	.85	.96	.96	.62	.96	.96	292.2 °K	CAE CHS SSC	72208 Charleston, SC
D, Bkn-Ovc Clouds	.84	.96	.96	.82	.96	.96	289.0 °K	NXX ABE	72407 Atlantic City, NJ

Table 9. Summary of the Model Radiance Calculation Input Parameters Used for Samples A-D. The Transmission Profiles for Each Sample Were Taken to be for a U.S. Standard Atmosphere (see Appendix A)

279.6	282.1	269.9	257.7
282.2	283.9	267.8	258.2
281.5	283.0	263.9	257.5
279.6	281.3	269.2	256.4
282.6	283.1	267.3	259.3
282.0	281.1	263.9	258.1
280.2	282.2	267.9	265.5
282.6	283.1	266.8	263.7
282.0	281.5	262.8	261.0
282.6	280.6	270.0	258.7
285.2	281.8	268.3	260.4
283.9	280.6	264.5	258.1

Ch 3
Ch 4
Ch 5

Legend

Figure 11a. Satellite-Observed Channel 3, 4, and 5 Brightness Temperatures T_{Br} (^{o}K) for Sample A

.50	0	.80	1.0
.5	0	3.5	4.5
0	0	.85	1.0
0	0	4	4.5
0	0	.70	.80
0	0	4.5	4.5
0	.05	.80	1.0
0	4	3.5	4.5

Cloud Amount ρ
Cloud Top Altitude z(km)

Legend

Figure 11b. Multispectral Cloud Analysis Model-Generated Cloud Amounts ρ ($0<\rho<1$) and Cloud Top Heights z (km) for Sample A

radiances and the Planck blackbody radiance function, and are not corrected for atmospheric attenuation, variations in emissivities from channel to channel, and so on. Note that Channel 3 brightness temperatures are colder than the Channel 4 brightness temperatures, on average. This is due to the fact that, although Channel 3 is a cleaner atmospheric window than is Channel 4, the shorter wavelength Channel 3 emissivities are significantly lower than both of the longer wavelength Channel 4 and Channel 5 emissivities, in turn making Channel 3's imagery appear slightly colder than Channel 4's (see Appendices A and B). Interestingly, on the other hand, Channel 5 brightness temperatures are frequently closer to those of Channel 3 due to the fact that, although Channel 3 emissivities are lower, Channel 5 is a relatively dirtier window in that it is much more sensitive to tropospheric water vapor attenuation.

The cloud cover and cloud top estimates obtained using the multispectral cloud analysis method are plotted in Figure 11b for Sample A. The model-estimated cloud amounts are consistent with the aforementioned subjective imagery analysis, and also agree with nearby surface weather station cloud cover observations which range anywhere from scattered ahead of the leading cloud edge (i.e., to the "left" of the sample) to broken/overcast coverage behind the cloud edge and in the clouds (i.e., to the "right" of the sample). Cloud base altitude reports of 7000 to 10000 feet (2 to 3 km), obtained from those same surface stations, also agree rather nicely with the model estimated cloud top altitudes plotted in Figure 11b. These results suggest cloud thicknesses for Sample A on the order of 3000 feet, which also seems intuitively reasonable on the basis of the surface observations and subjective satellite imagery impressions.

Sample B

The Sample B imagery, located over south central Canada, contains a solid low cloud band which is aligned from the lower left corner to the upper right corner of the 4 × 4 pixel array. The Channel 3, 4, and 5 brightness temperatures, plotted in Figure 12a, help confirm this subjective analysis. The model-estimated cloud amounts plotted in Figure 12b again appear reasonable, in light of both the imagery analysis and nearby surface cloud amount observations which range from scattered to broken coverage. The estimated cloud top heights correspond roughly well with surrounding observed cloud base heights on the order of 5000 feet (≈2 km).

Sample C

Sample C imagery lies near central South Carolina, and contains a very interesting low ground fog example. As previously mentioned in Part I, many times the difference between low cloud/fog and ground temperatures is not distinctive enough to affect a noticeable change in satellite-measured infrared radiances. Regions that appear cloud free in the IR imagery can often be cloud covered. The Channels 4 and 5 brightness temperatures for Sample C provide an excellent example of just such case. They are plotted in Figure 13a. Note that the pixel-to-pixel variations in T_{Br} for each of the long wavelength IR Channels 4 and 5 are at most on the order of 1 ^{o}K, a common variation for cloud free scenes. On the basis of this information alone, the image sample would appear to be clear.

However, note the significantly larger pixel-to-pixel variation among the Channel 3 satellite-measured brightness temperatures, which are more on the order of 5 ^{o}K, and are in stark contrast to the corresponding Channel 4 and Channel 5 T_{Br} variations. The cooler Channel 3 brightness temperatures (≈282 ^{o}K) are the foggy pixels, while the warmer brightness tem-

275.2	276.8	274.7	268.4
277.3	279.1	277.3	270.2
277.1	278.1	276.6	268.8
276.3	272.4	268.5	264.6
277.3	274.5	269.7	268.7
276.6	273.0	268.3	267.2
272.4	271.8	270.5	275.8
275.0	272.2	274.5	277.7
274.0	270.4	272.5	276.6
267.7	272.4	273.0	274.7
270.7	275.0	275.5	277.3
269.3	273.5	273.5	276.1

Ch 3
Ch 4
Ch 5

Legend

Figure 12a. Satellite-Observed Channel 3, 4, and 5 Brightness Temperatures T_{Br} (^{o}K) for Sample B

0	0	0	.9
0	0	0	2.5
0	.6	.8	.8
0	2	2.5	3
.8	.7	.8	0
1.5	2.5	2	0
.9	.75	.5	0
2.5	2	2	0

Cloud Amount ρ
Cloud Top Altitude z (km)

Legend

Figure 12b. Multispectral Cloud Analysis Model-Generated Cloud Amounts ρ ($0<\rho<1$) and Cloud Top Heights z (km) for Sample B

282.4 289.2 288.9	286.7 290.0 289.4	287.7 290.0 289.4	287.0 290.0 289.4
282.0 289.2 288.5	283.2 289.6 289.4	287.7 290.0 289.8	287.4 290.0 289.4
282.4 289.2 288.9	281.2 289.6 288.9	287.4 290.0 289.8	287.7 290.0 289.8
281.6 288.8 288.5	281.6 289.2 288.9	283.2 289.6 288.9	287.4 290.4 289.8

Ch 3
Ch 4
Ch 5

Legend

Figure 13a. Satellite-Observed Channel 3, 4, and 5 Brightness Temperatures T_{Br} (^{o}K) for Sample C

.95 0.5	0 0	0 0	0 0
.95 0.5	.90 0.5	0 0	0 0
.95 0.5	1.0 0.5	0 0	0 0
1.0 0.5	1.0 0.5	.85 0.5	0 0

Cloud Amount ρ

Cloud Top Altitude z (km)

Legend

Figure 13b. Multispectral Cloud Analysis Model-Generated Cloud Amounts ρ ($0<\rho<1$) and Cloud Top Heights z (km) for Sample C. The Hatched Area Indicates Where Subjective Imagery Analysis Locates the Fog

peratures (≈287 °K) are the clear pixels. The reason that Channel 3 does such a spectacular job in discriminating the ground fog contaminated pixels from the clear pixels of the imagery is due mainly to the fact that ground fog, which generally consists of very small water droplets, has an emissivity much lower than that of most land surfaces at 3.7μm, as is suggested in Appendix B. Recall from Table 9 that for Sample C a fog emissivity of .62 at 3.7μm was used, while a surface emissivity of .85 was used. This property makes the use of 3.7μm imagery in conjunction with Channel 4/5 imagery potentially indispensible for the detection of low nighttime ground fog. Detection of low fog at night is a recognized problem in operational cloud analysis techniques to date.

Figure 13b contains plots of the model estimated cloud parameters for Sample C. It is important to note that a large majority of the Channel 4 and Channel 5 observed radiances for Sample C indicated clear conditions when compared with the model computed radiances. Only the differnces in the Channel 3 radiance observations indicated the presence of fog. Note that both the model estimated cloud amounts and the cloud top altitudes show the fog to be quite uniform in both coverage and height (which in this case is precisely their thickness), on the order of 10/10 and 500 m, respectively. Note too the rather abrupt edge of the fog bank. These results are confirmed by the subjective imagery analysis; they certainly depict some of the more distinctive characteristics of nighttime ground fog.

Sample D

The Sample D imagery is situated near the central part of the New Jersey/Pennsylvania border, and contains a fairly homogeneous-looking broken/overcast cloud cover. A subjective imagery analysis hints at

either lower and/or fewer clouds in the extreme right side of the sample array, since in comparison to the leftmost three-fourths of the sample the right-hand grayshades are darker (warmer). Figure 14a plots the satellite observed brightness temperatures for Sample D, and the results of the cloud parameter multispectral analysis are plotted in Figure 14b. The model estimated cloud amounts shown in Figure 14b agree well with the nearby Willow Grove and Allentown, PA surface cloud amount observations (they report broken to overcast conditions for the image scene), and the estimated cloud top heights correspond well with the observed cloud base altitudes of 5000 to 7000 feet (2 km). These results indicate the average thickness of the cloud layer within Sample D to be on the order of 4000 feet.

IV. Concluding Remarks

The multispectral window channel cloud analysis algorithm described in this paper was tested on four imagery samples. Although the size of the sample set is obviously too small for firm conclusions, the test results do demonstrate the soundness of the approach and development of the theory and principles used in formulating the cloud analysis technique for NOAA AVHRR imagery, as described in Part II.

It is unrealistic to attempt to justify the success (or failure) of this multispectral technique on the basis of so few sample tests. Like many other automated satellite imagery classification techniques, "threshold" or otherwise, there are bound to be instances where this algorithm works extremely well (as the fog Sample C), and other instances where it works not so well. There is a high sensitivity of the accuracy of the cloud analysis model presented in this paper to effects such as varying

264.6 270.7 268.8	265.4 270.7 268.8	268.5 272.6 271.4	267.8 273.5 272.5
265.4 268.2 266.6	262.8 269.7 268.2	269.9 274.0 273.0	267.0 273.1 272.0
267.0 271.2 269.9	267.0 273.1 272.0	267.7 272.6 272.0	267.0 273.5 272.5
268.5 273.1 272.5	266.2 272.6 271.5	266.2 271.2 269.9	269.2 274.9 274.6

Ch 3
Ch 4
Ch 5

Legend

Figure 14a. Satellite-Observed Channel 3, 4, and 5 Brightness Temperatures T_{Br} (^{o}K) for Sample D

1.00 3.5	1.00 3.5	.95 3.5	.80 3.5
1.00 4	.95 4	.90 3	1.00 3
.90 3.5	1.00 3	.95 3.5	.80 3.5
.80 3.5	.95 3.5	.90 3.5	.80 3

Cloud Amount ρ
Cloud Top Altitude z(km)

Legend

Figure 14b. Multispectral Cloud Analysis Model-Generated Cloud Amounts ρ ($0<\rho<1$) and Cloud Top Heights z (km) for Sample D

surface emissivity, surface skin temperature estimates, and temperature and transmission profiles. Small uncertainties in any or all of these input parameters have the potential of yielding high uncertainties in the model analysis results. A list of potential problems with this cloud analysis technique are presented in Table 10, and discussed in the following paragraphs. The order of the listings is not meant to imply the importance of one particluar problem area over another.

1. Inaccuracies in the temperature profile for a particular scene will cause the greatest amount of error to be manifested in cloud top altitude analyses, with perhaps a more subtle effect on model generated cloud amounts. Effects of a bad temperature profile on the model computed atmospheric contribution to upwelling thermal radiance would probably be small in comparison to the surface-emitted radiance, since each of the three AVHRR channels are relatively clean atmospheric windows.

2. Surface skin temperature is one of the more crucial model input parameters to accurately specify, since it is this value that most of the satellite-observed AVHRR window radiances depend on. Clearly the bulk of clear column upwelling thermal radiance sensed in the AVHRR infrared window channels originates from the ground. Even for partly cloudy fields of view, the surface contribution to satellite-observed window radiances is generally quite significant due to the fact that the land backgrounds are usually warmer than the cloud tops.

3. Surface and cloud emissivities are difficult to specify accurately (see Appendix B). Aside from a dominant wavelength and surface type dependence, surface emissivities also vary on local and even subpixel scales due to effects such as variable soil moisture content, city/country mixed fields of view, vegetation type and cover, and even time of

1. Inaccuracy of the temperature, pressure profiles
2. Surface skin temperature specification
3. Uncertainty in surface emissivities and cloud emissivities
4. Cloud optical depths too low, cloud transmissivities too high
5. Calibration coefficients, AVHRR instrument noise
6. Inaccuracy of transmission profiles
7. Limb-viewing correction procedures
8. Localized surface inversions (espacially in Arctic regions), and low level fog

Table 10. List of Problem Areas to which the Multispectral Cloud Parameter Retrieval Method is Sensitive

day or year (e.g., deserts, snow/ice, tundra, ocean spray). Many models for cloud emissivities have been developed and tested over the years. (Results from some of them are tabulated in Appendix B.) Each model attempts to account for the microphysical properties of water droplets and ice particles in varying degrees of detail. Results from such studies generally indicate a complex dependence of low water cloud emissivities on droplet sizes, optical depths, and wavelength (Hunt, 1972). An attempt at a reasonable emissivity estimate for both the clouds and the underlying surface must be made, since the model generated clear/cloud radiances are sensitively dependent on the subtlest of cloud amount and cloud top altitude variations. Specification of surface and cloud emissivities on an interactive basis is not too easy; on an automated basis it is a difficult task indeed. However, it is important to somehow account for the fact that the surface and cloud emissivities are generally different from unity.

4. When using the multispectral cloud analysis technique, care must be exercised to insure that only thick (usually low-altitude water droplet) clouds lie within the sensor field of view. This is to ensure that the cloud optical depths are always high enough (i.e., that cloud transmissivities are low enough) that equation (16) does a good job in modeling upwelling radiance in the presence of a fractional or total cloud cover. If attempting to apply the cloud analysis presented here toward analysis of thinner clouds with high transmissivities (e.g., cirrus), then the satellite observed radiances whose fields of view contain these clouds would be significantly contaminated by emissions having originated from underlying surfaces. Model computed radiances using equation (16) do not account for this scheme.

5. Inaccurate calibration coefficients, along with sensor instrument

random noise, is always a condition that users of remotely sensed satellite data must be aware of. For the June 1982 time period of the data used in this study, sensor noise problems were at a relative minimum. Subjective analysis of the AVHRR imagery displays certainly hinted at no widespread or obvious instrument noise problems in any of the five window channels. However, as the summer of 1982 progressed, noise in Channel 3 gradually grew to become more and more of a problem until finally Channel 3 was ignored in NOAA sea-surface temperature estimates by October. (Random noise which increases with age of the Channel 3 sensor has been a common problem with all AVHRR instruments up to and including the NOAA-7 AVHRR.)

In addition, dust spewed from the El Chichon volcano in the spring of 1982 had noticeable effects on tropical satellite data, but the dust did not work its way up to midlatitudes until later that summer. (Volcanic dust is a significant scattering/absorbing atmospheric constituent of which users of satellite data must be aware.) For this particular study, which drew all of its imagery samples from the continental United States of America, volcanic dust posed no significant hindrance.

6. Transmission profiles depend upon the radiative properties and concentrations of atmospheric absorbers. Water vapor, a dominant tropospheric absorber at AVHRR window channel wavelengths, affects changes in atmospheric transmittances due to its variation in concentration from location to location. Transmittance functions vary as local absorber concentrations vary, so that in actuality the transmission profiles, even for atmospheric windows, vary locally as well. However, the dependence of atmospheric window transmissions on absorber concentrations is not nearly so strong as it is for opaque spectral regions (i.e., in absorption

bands). Thus all that appears necessary to adequately specify the AVHRR window transmission profiles for the model radiance cloud analysis technique is to use standard, climatological absorber concentration distributions to compute the window transmittances with. For this study, all the available transmittances in Appendix A were computed using either a climatological Arctic, U.S. Standard, or Tropical water vapor and ozone concentration profile. These three options cover dry, normal, and moist atmospheric conditions respectively, and in the testing stages of algorithm development it was up to the user to specify which of the aforementioned three possibilities was most appropriate for a particular image scene. Taking the transmittance profile to be that for a climatologically averaged atmosphere is not a severe assumption for window spectral regions. For the most part, transmittances in window regions are so close to unity and atmospheric contributions to upwelling radiance in window regions so small that using a climatological window spectral transmission profile is probably a very good assumption, and causes a minimal source of error in theoretical model computations of upwelling thermal window radiances.

7. Satellite sensors do not always "see" the same amounts of a cloud that a ground-based observer would see when reporting fractional cloud cover. This problem is enhanced for high satellite viewing angles, and results in the satellite's seeing more of the sides of clouds than does a surface observer when the clouds are directly over the observer. As a result, most automated satellite imagery classification techniques, including the one presented here will yield higher than actual cloud cover estimates for satellite data at the edge of scans than they will closer to the subpoint. Figure 15 depicts the geometry of this problem.

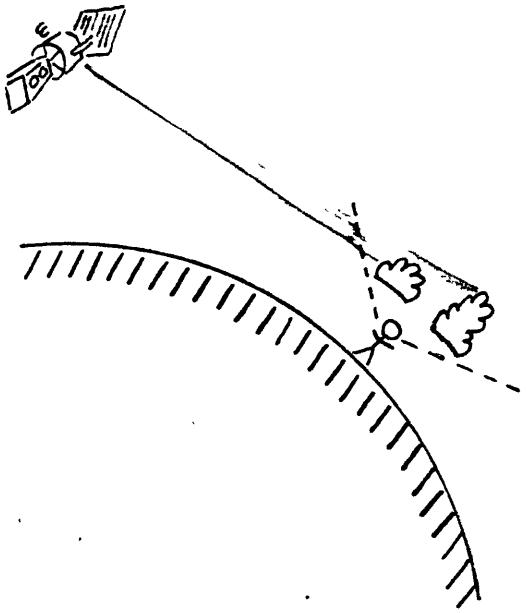

Figure 15. The Geometry for Clouds as Viewed at an Angle by Satellite and Those Same Clouds as Viewed by an Observer on the Ground Directly Beneath Those Clouds. In this Simple Illustration, the Ground-Based Observer Sees ≈60% Cloud Cover, While the Satellite Sensor Would Report 100% Cloud Cover

The effects of inflated satellite cloud-cover observations at scan edge are not negligible; indeed many statistical studies done over the past few years have shown a strong bias toward high cloud amounts at high viewing angles. When applying the multispectral cloud analysis to scenes at large viewing angles, this high cloud cover bias must be kept in mind while attempting to compare surface-based cloud cover observations to model generated cloud amount estimates. Perhaps the best way to account for satellite overspecification of cloud amount is to apply some sort of a statistically-based downward correction to the satellite imagery-derived cloud covers.

8. One recognized problem for "threshold" image analysis techniques (threshold methods are described in Part I) is how to detect the presence of low-level cloud in the presence of a strong temperature inversion. Shallow inversions are quite common globally, and especially so during nighttime hours, and present a real difficulty for low-level cloud analyses using satellite imagery. When a threshold technique compares a satellite measured brightness temperature T_{Br} to an observed ground (skin) temperature T_{sfc}, it checks to see whether T_{Br} is greater or less than T_{sfc}. If $T_{sfc} > T_{Br}$ by a predefined threshold amount, then the field of view is considered cloud contaminated. For most situations this is a reasonable assumption. However for clouds whose tops lie in an inversion, $T_{Br} > T_{sfc}$ and the field of view is flagged by the threshold method as cloud free. However, the multispectral cloud analysis technique presented in this study will at least be able to attempt a comparison of the satellite observed radiance values with theoretically computed values which take into account the fact that a cloud might lie within an inversion. This fact alone greatly increases the chance of a low cloud or fog

layer's being detected.

In summary, the multispectral cloud parameter retrieval method described in this paper has been demonstrated as a promising technique which uses NOAA polar orbiter nighttime AVHRR measurements to determine cloud amount and cloud top heights of lower level tropospheric clouds. There are certainly easier ways to detect the presence of most of the clouds encountered in satellite imagery; cloud top temperatures by and large are significantly colder than surface background temperatures so as to allow for their detection by even the simplest of single window IR threshold techniques. However, one of the real advantages of the multispectral AVHRR cloud analysis technique lies in its more physically sound approach in determining cloud amounts and cloud top altitudes.

Single IR window approaches toward detection of clouds and specification of cloud coverage are severely restricted in their ability to detect sub-pixel resolution clouds. When a threshold technique flags a satellite brightness temperature as cloud contaminated, it is forced to assume that clouds completely fill the sensor's field of view. Subsequently, cloud amounts over some geographical area are forced to be computed as the ratio of cloudy pixels to the total number of pixels covering that geographical area. By its very definition, cloud amounts computed in this fashion are only an average estimate of expected cloud cover valid over a given geographical region. As a result, single window threshold techniques tend to overestimate cloud areal coverage and underestimate the cloud top altitudes of pixels whose fields of view contain sub-pixel resolution cloud elements. However, the multispectral imagery analysis technique demonstrated in this study possesses the capability of detecting sub-pixel resolution cloud amounts, and hence offers a more

physically attractive alternative toward the specification of satellite-based fractional cloud cover and cloud top altitudes of such clouds. This characteristic makes worthwhile the increase in algorithm complexity and computational time brought on by the application of the multispectral cloud analysis method. An increase in the accuracy of satellite based information concerning cloud cover and cloud tops would greatly enhance the ability of medium range and climate modelers to assess the important long term role played by low-level clouds play in earth boundary layer radiation processes and climate dynamics.

As is the case with nearly any satellite imagery cloud classification scheme, there are certainly many ways in which the multispectral cloud analysis technique presented here can be streamlined into an effective automated cloud analysis procedure. A unique feature of this technique is that it breaks the more traditional barrier of "threshold" cloud analysis methods in providing a more physically sound process through which cloud amount and cloud top altitudes can be determined. On the basis of this study's results, the multispectral cloud analysis method has been demonstrated as a feasible nighttime imagery classification technique. But as with any technique, its ultimate accuracy and reliability must be determined through future experiments using a much broader, more diverse set of AVHRR nighttime image samples.

V. References

Arking, Albert and Childs, Jeffrey D., 1983: "Extraction of Cloud Cover Parameters From Multispectral Satellite Measurements." Proc. Fifth Conference on Atmospheric Radiation, Baltimore, 31 Oct - 4 Nov 1983. Amer. Meteor. Soc., pp. 258-263.

Coakley, J. A., Jr. and Baldwin, D. G., 1983: "Towards the Objective Analysis of Clouds From Satellite Imagery Data." Submitted for publ. Journ. of Clim. and Appl. Meteor.

Colwell, Robert N. (ed.), 1983: "Manual of Remote Sensing. Volume I: Theory, Instruments, and Techniques." Amer. Soc. of Photogrammetry, Falls Church, VA, pp. 94-95.

Dozier, Jeff, 1981: "A Method for Satellite Identification of Surface Temperature Fields of Subpixel Resolution." Remote Sensing of Environ., 11, No. 3, pp. 221-229.

Henderson-Sellers, A. and Hughes, N. A., 1983: "A Preliminary Investigation of the Hazards of Comparing Model and Observed Cloud Climatologies." (submitted for publ. to Journ. of Climat.)

Hunt, G. E., 1972: "Radiative Properties of Terrestrial Clouds at Visible and Infra-Red Thermal Window Wavelengths." Quart. Journ. Royal Meteor. Soc. (1973), 99, pp. 346-369.

Jacobowitz, H. and Smith, W. L., 1974: "The Difference in the Radiative Properties of Clouds for the 3.8 and 11 μm Window Regions and its Effect on the Determination of Sea Surface Temperatures." NOAA Technical Memorandum, U.S. Department of Commerce, Miami, 11 pp.

Kidwell, Katherine B. (ed.), 1983: "NOAA Polar Orbiter Data (TIROS-N, NOAA-6, NOAA-7, and NOAA-8) User's Guide." NOAA/NESDIS publ., 114 pp.

Lauritson, Levin, Nelson, Gary J. and Porto, Frank W., 1979: "Data Extraction and Calibration of TIROS-N/NOAA Radiometers." NOAA Tech. Memorandum NESS 107, U.S. Department of Commerce, Miami, 58 pp.

Liou, Kuo-Nan, 1980: An Introduction to Atmospheric Radiation. Academic Press, 392 pp.

McClain, E. Paul, 1981: "Multiple Atmospheric-Window Techniques for Satellite-Derived Sea Surface Temperatures." Oceanography from Space, Plenum Publ. Corp., pp. 73-85.

McClatchey, R. A. et al, 1972: "Optical Properties of the Atmosphere (Third Edition)." Air Force Cambridge Research Laboratories AFCRL-72-0497, 108 pp.

Prinn, Ronald G.: "Atmospheric Radiation." Massachusetts Institute of

Technology, Department of Earth, Atmospheric, and Planetary Sciences course notes.

Selby, J. E. A. and McClatchey, Robert A., 1975: "Atmospheric Transmittance From 0.25 to 28.5μm: Computer Code LOWTRAN 3." Air Force Cambridge Research Laboratories AFCRL-TR-75-0255, 109 pp.

Smith, W. L. and Rao, P. K., 1972: "The Determination of Surface Temperature From Satellite 'Window' Radiation Measurements." Temperature: Its Measurement and Control in Science and Industry, 4, Part 3. Instrument Soc. of Amer., pp. 2251-2257.

Wielicki, Bruce A. and Coakley, James A., Jr., 1981: "Cloud Retrieval Using Infrared Sounder Data: Error Analysis." Journ. Appl. Meteor., 20, pp. 157-169.

VI. Appendices

Appendix A

In this appendix are listed the results of the transmittance computations for each of the three thermal infrared AVHRR window channels 3, 4, and 5. The transmittances were calculated using AFGL's computer code RSAT (personal communication, Dr. Robert A. McClatchey). RSAT is designed to calculate atmospheric spectral transmission functions as defined by equation (12a), and takes into account absorption by well mixed gases, water vapor, ozone, and the effects of varying satellite viewing angle (which determines optical path length). Tables A1, A2, and A3 list the three model atmospheres Subarctic Winter, U.S. Standard, and Tropical used as a basis for the computations of the atmospheric spectral transmittances, which are listed in Tables A4 - A18.

SUBARCTIC WINTER					
Ht. (km)	Pressure (mb)	Temp. (°K)	Density (g/m^3)	Water Vapor (g/m^3)	Ozone (g/m^3)
0	1.013E+03	257.1	1.372E+03	1.2E+00	4.1E-05
1	8.878E+02	259.1	1.193E+03	1.2E+00	4.1E-05
2	7.775E+02	255.9	1.058E+03	9.4E-01	4.1E-05
3	6.798E+02	252.7	9.366E+02	6.8E-01	4.3E-05
4	5.932E+02	247.7	8.339E+02	4.1E-01	4.5E-05
5	5.158E+02	240.9	7.457E+02	2.0E-01	4.7E-05
6	4.467E+02	234.1	6.646E+02	9.8E-02	4.9E-05
7	3.853E+02	227.3	5.904E+02	5.4E-02	7.1E-05
8	3.308E+02	220.6	5.226E+02	1.1E-02	9.0E-05
9	2.829E+02	217.2	4.538E+02	8.4E-03	1.6F-04
10	2.418E+02	217.2	3.879E+02	5.5E-03	2.4E-04
11	2.067E+02	217.2	3.315E+02	3.8E-03	3.2E-04
12	1.766F+02	217.2	2.834E+02	2.6E-03	4.3E-04
13	1.510E+02	217.2	2.422E+02	1.8E-03	4.7E-04
14	1.291E+02	217.2	2.071E+02	1.0E-03	4.9E-04
15	1.103E+02	217.2	1.770E+02	7.6E-04	5.6E-04
16	9.431E+01	216.6	1.517E+02	6.4E-04	6.2E-04
17	8.058E+01	216.0	1.300E+02	5.6E-04	6.2E-04
18	6.882E+01	215.4	1.113E+02	5.0E-04	6.2E-04
19	5.875E+01	214.8	9.529E+01	4.9E-04	6.0E-04
20	5.014E+01	214.1	8.155E+01	4.5E-04	5.6E-04
21	4.277E+01	213.6	6.976E+01	5.1E-04	5.1E-04
22	3.647E+01	213.0	5.966E+01	5.1E-04	4.7E-04
23	3.109E+01	212.4	5.100E+01	5.4E-04	4.3E-04
24	2.649E+01	211.8	4.358E+01	6.0E-04	3.6E-04
25	2.256E+01	211.2	3.722E+01	6.7E-04	3.2E-04
30	1.020E+01	216.0	1.645E+01	3.6E-04	1.5E-04
35	4.701E+00	222.2	7.368E+00	1.1E-04	9.2E-05
40	2.243E+00	234.7	3.330E+00	4.3E-05	4.1E-05
45	1.113E+00	247.0	1.569E+00	1.9E-05	1.3E-05
50	5.719E-01	259.3	7.682E-01	6.3E-06	4.3E-06
70	4.016E-02	245.7	5.695E-02	1.4E-07	8.6E-08
100	3.000E-04	210.0	5.000E-04	1.0E-09	4.3E-11

Table A1. Subarctic Winter Model Atmosphere Used as a Basis for the Computation of Atmospheric Transmittance (after McClatchey et al, 1972)

U. S. STANDARD ATMOSPHERE, 1962					
Ht. (km)	Pressure (mb)	Temp. (^{o}K)	Density (g/m^3)	Water Vapor (g/m^3)	Ozone (g/m^3)
0	1.013E+03	288.1	1.225E+03	5.9E+00	5.4E-05
1	8.986E+02	281.6	1.111E+03	4.2E+00	5.4E-05
2	7.950E+02	275.1	1.007E+03	2.9E+00	5.4E-05
3	7.012E+02	268.7	9.093E+02	1.8E+00	5.0E-05
4	6.166E+02	262.2	8.193E+02	1.1E+00	4.6E-05
5	5.405E+02	255.7	7.364E+02	6.4E-01	4.5E-05
6	4.722E+02	249.2	6.601E+02	3.8E-01	4.5E-05
7	4.111E+02	242.7	5.900E+02	2.1E-01	4.8E-05
8	3.565E+02	236.2	5.258E+02	1.2E-01	5.2E-05
9	3.080E+02	229.7	4.671E+02	4.6E-02	7.1E-05
10	2.650E+02	223.2	4.135E+02	1.8E-02	9.0E-05
11	2.270E+02	216.8	3.648E+02	8.2E-03	1.3E-04
12	1.940E+02	216.6	3.119E+02	3.7E-03	1.6E-04
13	1.658E+02	216.6	2.666E+02	1.8E-03	1.7E-04
14	1.417E+02	216.6	2.279E+02	8.4E-04	1.9E-04
15	1.211E+02	216.6	1.948E+02	7.2E-04	2.1E-04
16	1.035E+02	216.6	1.665E+02	6.1E-04	2.3E-04
17	8.850E+01	216.6	1.423E+02	5.2E-04	2.8E-04
18	7.565E+01	216.6	1.216E+02	4.4E-04	3.2E-04
19	6.467E+01	216.6	1.040E+02	4.4E-04	3.5E-04
20	5.529E+01	216.6	8.891E+01	4.4E-04	3.8E-04
21	4.729E+01	217.6	7.572E+01	4.8E-04	3.8E-04
22	4.047E+01	218.6	6.451E+01	5.2E-04	3.9E-04
23	3.467E+01	219.6	5.500E+01	5.7E-04	3.8E-04
24	2.972E+01	220.6	4.694E+01	6.1E-04	3.6E-04
25	2.549E+01	221.6	4.008E+01	6.6E-04	3.4E-04
30	1.197E+01	226.5	1.841E+01	3.8E-04	2.0E-04
35	5.746E+00	236.5	8.463E+00	1.6E-04	1.1E-04
40	2.871E+00	250.4	3.996E+00	6.7E-05	4.9E-05
45	1.491E+00	264.2	1.966E+00	3.2E-05	1.7E-05
50	7.978E-01	270.6	1.027E+00	1.2E-05	4.0E-06
70	5.520E-02	219.7	8.754E-02	1.5E-07	8.6E-08
100	3.008E-04	210.0	4.989E-04	1.0E-09	4.3E-11

Table A2. U.S. Standard Model Atmosphere Used as a Basis for the Computation of Atmospheric Transmittance (after McClatchey et al, 1972)

TROPICAL					
Ht. (km)	Pressure (mb)	Temp. (°K)	Density (g/m^3)	Water Vapor (g/m^3)	Ozone (g/m^3)
0	1.013E+03	300.0	1.167E+03	1.9E+01	5.6E-05
1	9.040E+02	294.0	1.064E+03	1.3E+01	5.6E-05
2	8.050E+02	288.0	9.689E+02	9.3E+00	5.4E-05
3	7.150E+02	284.0	8.756E+02	4.7E+00	5.1E-05
4	6.330E+02	277.0	7.951E+02	2.2E+00	4.7E-05
5	5.590E+02	270.0	7.199E+02	1.5E+00	4.5E-05
6	4.920E+02	264.0	6.501E+02	8.5E-01	4.3E-05
7	4.320E+02	257.0	5.855E+02	4.7E-01	4.1E-05
8	3.780E+02	250.0	5.258E+02	2.5E-01	3.9E-05
9	3.290E+02	244.0	4.708E+02	1.2E-01	3.9E-05
10	2.860E+02	237.0	4.202E+02	5.0E-02	3.9E-05
11	2.470E+02	230.0	3.740E+02	1.7E-02	4.1E-05
12	2.130E+02	224.0	3.316E+02	6.0E-03	4.3E-05
13	1.820E+02	217.0	2.929E+02	1.8E-03	4.5E-05
14	1.560E+02	210.0	2.578E+02	1.0E-03	4.5E-05
15	1.320E+02	204.0	2.260E+02	7.6E-04	4.7E-05
16	1.110E+02	197.0	1.972E+02	6.4E-04	4.7E-05
17	9.370E+01	195.0	1.676E+02	5.6E-04	6.9E-05
18	7.890E+01	199.0	1.382E+02	5.0E-04	9.0E-05
19	6.660E+01	203.0	1.145E+02	4.9E-04	1.4E-04
20	5.650E+01	207.0	9.515E+01	4.5E-04	1.9E-04
21	4.800E+01	211.0	7.938E+01	5.1E-04	2.4E-04
22	4.090E+01	215.0	6.645E+01	5.1E-04	2.8E-04
23	3.500E+01	217.0	5.618E+01	5.4E-04	3.2E-04
24	3.000E+01	219.0	4.763E+01	6.0E-04	3.4E-04
25	2.570E+01	221.0	4.045E+01	6.7E-04	3.4E-04
30	1.220E+01	232.0	1.831E+01	3.6E-04	2.4E-04
35	6.000E+00	243.0	8.600E+00	1.1E-04	9.2E-05
40	3.050E+00	254.0	4.181E+00	4.3E-05	4.1E-05
45	1.590E+00	265.0	2.097E+00	1.9E-05	1.3E-05
50	8.540E-01	270.0	1.101E+00	6.3E-06	4.3E-06
70	5.790E-02	219.0	9.210E-02	1.4E-07	8.6E-08
100	3.000E-04	210.0	5.000E-04	1.0E-09	4.3E-11

Table A3. Tropical Model Atmosphere Used as a Basis for the Computation of Atmospheric Transmittance (after McClatchey et al, 1972)

HEIGHT (KM)	TRANSMITTANCE TROPICAL	US STANDARD	SUBARCTIC WINTER
70	.99999	.99999	.99999
50	.99998	.99998	.99998
25	.99953	.99953	.99959
20	.99802	.99885	.99896
15	.99681	.99715	.99744
10	.99189	.99272	.99351
9	.99003	.99119	.99219
8	.98735	.98917	.99063
7	.98340	.98642	.98874
6	.97744	.98266	.98634
5	.96829	.97737	.98327
4	.95521	.96973	.97901
3	.93448	.95859	.97302
2	.89800	.94253	.96511
1	.84664	.92056	.95538
0	.78214	.89220	.94456

TABLE A4. ATMOSPHERIC SPECTRAL TRANSMITTANCE PROFILES FOR NOAA-7 AVHRR CHANNEL 3, SATELLITE VIEWING ANGLE 0 DEG

HEIGHT (KM)	TRANSMITTANCE TROPICAL	US STANDARD	SUBARCTIC WINTER
70	.99999	.99999	.99999
50	.99998	.99998	.99998
25	.99943	.99943	.99951
20	.99857	.99860	.99875
15	.99613	.99653	.99689
10	.99014	.99114	.99210
9	.98789	.98928	.99050
8	.98464	.98684	.98860
7	.97989	.98351	.98631
6	.97276	.97897	.98341
5	.96190	.97261	.97969
4	.94653	.96349	.97456
3	.92246	.95030	.96734
2	.88082	.93145	.95787
1	.82302	.90595	.94628
0	.75021	.87339	.93345

TABLE A5. ATMOSPHERIC SPECTRAL TRANSMITTANCE PROFILES FOR NOAA-7 AVHRR CHANNEL 3, SATELLITE VIEWING ANGLE 30 DEG

HEIGHT (KM)	TRANSMITTANCE TROPICAL	US STANDARD	SUBARCTIC WINTER
70	.99999	.99999	.99999
50	.99997	.99996	.99996
25	.99922	.99921	.99931
20	.99814	.99818	.99837
15	.99509	.99558	.99603
10	.98757	.98882	.99003
9	.98475	.98649	.98802
8	.98070	.98344	.98566
7	.97480	.97929	.98280
6	.96598	.97365	.97918
5	.95269	.96578	.97456
4	.93410	.95457	.96818
3	.90545	.93852	.95923
2	.85685	.91588	.94757
1	.78921	.88567	.93339
0	.70669	.84761	.91779

TABLE A6. ATMOSPHERIC SPECTRAL TRANSMITTANCE PROFILES FOR NOAA-7 AVHRR CHANNEL 3, SATELLITE VIEWING ANGLE 40 DEG

HEIGHT (KM)	TRANSMITTANCE TROPICAL	US STANDARD	SUBARCTIC WINTER
70	.99999	.99999	.99999
50	.99994	.99993	.99993
25	.99887	.99887	.99901
20	.99742	.99747	.99773
15	.99330	.99394	.99457
10	.98326	.98490	.98652
9	.97952	.98181	.98386
8	.97417	.97777	.98073
7	.96641	.97228	.97696
6	.95495	.96487	.97219
5	.93790	.95458	.96611
4	.91450	.94009	.95773
3	.87922	.91962	.94604
2	.82073	.89125	.93093
1	.74041	.85410	.91274
0	.64422	.80811	.89293

TABLE A7. ATMOSPHERIC SPECTRAL TRANSMITTANCE PROFILES FOR NOAA-7 AVHRR CHANNEL 3, SATELLITE VIEWING ANGLE 50 DEG

HEIGHT (KM)	TRANSMITTANCE TROPICAL	US STANDARD	SUBARCTIC WINTER
70	.99999	.99999	.99999
50	.99992	.99991	.99991
25	.99847	.99847	.99867
20	.99657	.99664	.99699
15	.99124	.99206	.99288
10	.97843	.98049	.98256
9	.97368	.97658	.97919
8	.96688	.97145	.97523
7	.95707	.96451	.97049
6	.94271	.95515	.96448
5	.92615	.94225	.95680
4	.89325	.92426	.94623
3	.85132	.89920	.93154
2	.78176	.86507	.91269
1	.68902	.82112	.89025
0	.58168	.76754	.86606

TABLE A8. ATMOSPHERIC SPECTRAL TRANSMITTANCE PROFILES FOR NOAA-7 AVHRR CHANNEL 3, SATELLITE VIEWING ANGLE 55 DEG

HEIGHT (KM)	TRANSMITTANCE TROPICAL	US STANDARD	SUBARCTIC WINTER
70	.99999	.99999	.99999
50	.99998	.99998	.99998
25	.99992	.99993	.99996
20	.99986	.99985	.99991
15	.99974	.99965	.99973
10	.99892	.99907	.99923
9	.99833	.99879	.99906
8	.99724	.99828	.99886
7	.99523	.99737	.99855
6	.99144	.99576	.99801
5	.98436	.99288	.99708
4	.97215	.98770	.99533
3	.94603	.97824	.99211
2	.87239	.96093	.98702
1	.72865	.93099	.97989
0	.53048	.88348	.97154

TABLE A9. ATMOSPHERIC SPECTRAL TRANSMITTANCE PROFILES FOR NOAA-7 AVHRR CHANNEL 4, SATELLITE VIEWING ANGLE 0 DEG

HEIGHT (KM)	TRANSMITTANCE TROPICAL	US STANDARD	SUBARCTIC WINTER
70	.99999	.99999	.99999
50	.99998	.99998	.99998
25	.99991	.99992	.99996
20	.99983	.99983	.99989
15	.99969	.99958	.99967
10	.99871	.99889	.99907
9	.99801	.99855	.99888
8	.99671	.99795	.99863
7	.99432	.99685	.99826
6	.98987	.99494	.99761
5	.98158	.99153	.99650
4	.96730	.98543	.99440
3	.93664	.97433	.99054
2	.85051	.95400	.98446
1	.68631	.91886	.97598
0	.47000	.86333	.96606

TABLE A10. ATMOSPHERIC SPECTRAL TRANSMITTANCE PROFILES FOR NOAA-7 AVHRR CHANNEL 4, SATELLITE VIEWING ANGLE 30 DEG

HEIGHT (KM)	TRANSMITTANCE TROPICAL	US STANDARD	SUBARCTIC WINTER
70	.99999	.99999	.99999
50	.99997	.99997	.99997
25	.99989	.99990	.99994
20	.99979	.99978	.99986
15	.99961	.99947	.99959
10	.99838	.99861	.99884
9	.99750	.99819	.99860
8	.99588	.99743	.99829
7	.99292	.99607	.99782
6	.98748	.99369	.99701
5	.97742	.98949	.99562
4	.96006	.98203	.99300
3	.92270	.96850	.98822
2	.81880	.94371	.98075
1	.62741	.90097	.97035
0	.39208	.83417	.95821

TABLE A11. ATMOSPHERIC SPECTRAL TRANSMITTANCE PROFILES FOR NOAA-7 AVHRR CHANNEL 4, SATELLITE VIEWING ANGLE 40 DEG

HEIGHT (KM)	TRANSMITTANCE TROPICAL	US STANDARD	SUBARCTIC WINTER
70	.99999	.99999	.99999
50	.99994	.99995	.99997
25	.99985	.99987	.99993
20	.99971	.99971	.99982
15	.99948	.99929	.99945
10	.99782	.99814	.99844
9	.99665	.99757	.99812
8	.99451	.99656	.99771
7	.99063	.99475	.99709
6	.98361	.99161	.99600
5	.97072	.98615	.99414
4	.94837	.97651	.99068
3	.90026	.95908	.98440
2	.76932	.92707	.97465
1	.54132	.87222	.96113
0	.29074	.78813	.94536

TABLE A12. ATMOSPHERIC SPECTRAL TRANSMITTNACE PROFILES FOR NOAA-7 AVHRR CHANNEL 4, SATELLITE VIEWING ANGLE 50 DEG

HEIGHT (KM)	TRANSMITTANCE TROPICAL	US STANDARD	SUBARCTIC WINTER
70	.99999	.99999	.99999
50	.99994	.99994	.99994
25	.99980	.99982	.99990
20	.99962	.99962	.99976
15	.99933	.99908	.99928
10	.99718	.99759	.99798
9	.99567	.99686	.99756
8	.99293	.99556	.99704
7	.98803	.99324	.99624
6	.97927	.98925	.99484
5	.96317	.98236	.99245
4	.93511	.97029	.98803
3	.87502	.94839	.98006
2	.71500	.90820	.96776
1	.45459	.84003	.95073
0	.20381	.73763	.93087

TABLE A13. ATMOSPHERIC SPECTRAL TRANSMITTANCE PROFILES FOR NOAA-7 AVHRR CHANNEL 4, SATELLITE VIEWING ANGLE 55 DEG

HEIGHT (KM)	TRANSMITTANCE TROPICAL	US STANDARD	SUBARCTIC WINTER
70	.99999	.99999	.99999
50	.99997	.99997	.99998
25	.99995	.99995	.99997
20	.99991	.99990	.99993
15	.99985	.99980	.99984
10	.99932	.99950	.99960
9	.99866	.99927	.99951
8	.99712	.99871	.99940
7	.99384	.99747	.99917
6	.98720	.99502	.99862
5	.97441	.99026	.99749
4	.95276	.98124	.99491
3	.90902	.96453	.98964
2	.79651	.93470	.98105
1	.59983	.88591	.96902
0	.36734	.81318	.95531

TABLE A14. ATMOSPHERIC SPECTRAL TRANSMITTANCE PROFILES FOR NOAA-7 AVHRR CHANNEL 5, SATELLITE VIEWING ANGLE 0 DEG

HEIGHT (KM)	TRANSMITTANCE TROPICAL	US STANDARD	SUBARCTIC WINTER
70	.99999	.99999	.99999
50	.99996	.99996	.99998
25	.99993	.99994	.99996
20	.99989	.99988	.99992
15	.99982	.99976	.99981
10	.99918	.99939	.99952
9	.99839	.99912	.99941
8	.99657	.99846	.99928
7	.99270	.99699	.99900
6	.98495	.99408	.99835
5	.97014	.98847	.99700
4	.94528	.97794	.99394
3	.89507	.95858	.98771
2	.76610	.92421	.97762
1	.54763	.86821	.96357
0	.30629	.78534	.94757

TABLE A15. ATMOSPHERIC SPECTRAL TRANSMITTANCE PROFILES FOR NOAA-7 AVHRR CHANNEL 5, SATELLITE VIEWING ANGLE 30 DEG

HEIGHT (KM)	TRANSMITTANCE TROPICAL	US STANDARD	SUBARCTIC WINTER
70	.99999	.99999	.99999
50	.99996	.99996	.99998
25	.99992	.99992	.99995
20	.99986	.99985	.99990
15	.99977	.99970	.99977
10	.99899	.99925	.99940
9	.99801	.99891	.99927
8	.99577	.99809	.99910
7	.99105	.99628	.99877
6	.98172	.99271	.99796
5	.96410	.98588	.99628
4	.93472	.97321	.99252
3	.87520	.95009	.98490
2	.72387	.90929	.97265
1	.47891	.84297	.95568
0	.23422	.74612	.93649

TABLE A16. ATMOSPHERIC SPECTRAL TRANSMITTANCE PROFILES FOR NOAA-7 AVHRR CHANNEL 5, SATELLITE VIEWING ANGLE 40 DEG

HEIGHT (KM)	TRANSMITTANCE TROPICAL	US STANDARD	SUBARCTIC WINTER
70	.99999	.99999	.99999
50	.99994	.99995	.99998
25	.99989	.99990	.99994
20	.99982	.99981	.99987
15	.99971	.99961	.99969
10	.99867	.99901	.99921
9	.99739	.99857	.99904
8	.99448	.99750	.99882
7	.98841	.99512	.99838
6	.97664	.99050	.99732
5	.95474	.98176	.99512
4	.91838	.96573	.99021
3	.84461	.93683	.98039
2	.66000	.88615	.96474
1	.38462	.80435	.94329
0	.15090	.68709	.91917

TABLE A17. ATMOSPHERIC SPECTRAL TRANSMITTANCE PROFILES FOR NOAA-7 AVHRR CHANNEL 5, SATELLITE VIEWING ANGLE 50 DEG

HEIGHT (KM)	TRANSMITTANCE TROPICAL	US STANDARD	SUBARCTIC WINTER
70	.99999	.99999	.99999
50	.99993	.99994	.99998
25	.99987	.99987	.99992
20	.99977	.99976	.99983
15	.99963	.99950	.99960
10	.97830	.99874	.99899
9	.99666	.99817	.99878
8	.99297	.99680	.99849
7	.98540	.99378	.99793
6	.97095	.98794	.99656
5	.94435	.97707	.99375
4	.90009	.95736	.98751
3	.81038	.92207	.97516
2	.59247	.86017	.95570
1	.29733	.76135	.92923
0	.08994	.62379	.89963

TABLE A18. ATMOSPHERIC SPECTRAL TRANSMITTANCE PROFILES FOR NOAA-7 AVHRR CHANNEL 5, SATELLITE VIEWING ANGLE 55 DEG

Appendix B

In this appendix are listed several tables of emissivities for several cloud types and surface types at the 3.7μm (AVHRR Channel 3) and 11μm (Channels 4/5) wavelength spectral regions.

Emissivities are a function of satellite viewing angle, wavelength, and temperature of the emitting surface element. Under carefully controlled laboratory conditions, emissivity measurements of small samples of polished minerals or powders are easily made. However, few measurements of emissivities for terrestrial backgrounds such as forests, tundra, farms, and deserts, are available. Even if they were, such emissivity measurements are highly dependent upon the natural variability of the targets encountered, along with the complex radiative properties of their component constituents and how each of them contribute to overall target emissivities. Directional dependencies of emissivity are generally assumed to be small (Colwell (ed.), 1983). Nonetheless, accurate specification of emissivities for terrestrial backgrounds is a difficult problem at best, and comprises a whole science in itself.

Table B1 lists some examples of integrated spectral emissivities of various surface types over two wavelength bands, one in the near-infrared and one in the thermal infrared. Tables B2 and B3 list emissivities for similar wavelength intervals for water clouds with various spherical droplet sizes. The emissivity values listed in these tables helped to provide a best estimate for the emissivities used in the multispectral radiance calculations (as defined by equation (16)). Note in general that near-infrared 3.7μm emissivities are lower than 11μm emissivities, thus tending to make AVHRR 3.7μm Channel 3 imagery appear colder than corresponding 10.7μm Channel 4 imagery, even though Channel 3 is a cleaner atmospheric

Feature	Emissivity by Wavelength band, μm	
	3.0–5.5	8.0–14.0
Green mountain laurel	0.90	0.92
Young willow leaf (dry, top)	0.94	0.96
Holly leaf (dry, top)	0.90	0.90
Holly leaf (dry, bottom)	0.86	0.94
Pressed dormant maple leaf (dry, top)	0.87	0.92
Grean leaf winter color—oak leaf (dry, top)	0.90	0.92
Green coniferous twigs (jack pine)	0.96	0.97
Grass—meadow fescue (dry)	0.82	0.88
Bark—northern red oak	0.90	0.96
Bark—northern American jack pine	0.88	0.97
Bark—Colorado spruce	0.87	0.94
Corn		0.94
Indian-fis cactus		0.96
Prickly pear cactus		0.96
Cotton (upland)		0.96
Tobacco		0.97
Blind-pear cactus		0.98
Fremont cottonwood		0.98
Philodendron		0.99
Sugarcane		0.99

Table B1. Integrated Emissivities of Some Representative Vegetation Materials in Two Wavelength Regions (after Colwell, 1983)

Drop Size Distribution: r_{low} = .01μm, r_{hi} = 10μm, r_c = 4μm
(Smaller Droplets)

Optical Depth τ_λ	Emissivity ε_λ	Transmissivity t_λ	Reflectivity r_λ
.01	.005	.988	.007
.5	.029	.939	.032
1	.061	.876	.063
2	.13	.75	.12
3	.21	.63	.16
5	.35	.44	.21
10	.58	.17	.25
50	.74	.00007	.25993
100	.74	—	.26

Drop Size Distrubution: r_{low} = .01μm, r_{hi} = 20μm, r_c = 10μm
(Larger Droplets)

Optical Depth τ_λ	Emissivity ε_λ	Transmissivity t_λ	Reflectivity r_λ
.1	.012	.984	.004
.5	.063	.919	.018
1	.13	.84	.03
5	.56	.35	.09
10	.80	.10	.10
50	.90	—	.10
100	.90	—	.10

Table B2. List of Emissivities, Transmissivities, and Reflectivities as a Function of Optical Depth at λ = 3.8μm for Two Spherical Water Droplet Size Distributions. r_{low} is the Lower Bound, r_{hi} is the Upper Bound, and r_c is the Central Mode of the Disribution. Note How Emissivities at 3.8μm Decrease as Droplet Size Decreases (from Hunt, 1972)

Drop Size Distribution: r_{low} = 1μm, r_{hi} = 100μm, r_c = 50μm

Optical Depth τ_λ	Emissivity ε_λ	Transmissivity t_λ	Reflectivity r_λ
0.1	.05	.95	—
.5	.22	.78	—
1	.39	.61	—
5	.92	.08	—
10	.991	.006	.003
50	.997	—	.003
100	.997	—	.003

Table B3. List of Emissivities, Transmissivities, and Reflectivities for Various Optical Depths at λ = 11μm. r_{low}, r_{hi}, and r_c Are as for Table B2. Note the Reflectivities r_λ at 11μm are Very Small in Comparison to Corresponding Reflectivities at λ = 3.8μm (from Hunt, 1972)

window region. Perhaps the only exception to this general rule of thumb is for calm, clear ocean scenes where 3.7μm satellite brightness temperatures can meet and even exceed those at 11μm.

VII. Glossary of Symbols

$B_\lambda(T)$ Planck blackbody radiance ([Energy per unit time per unit area per unit wavelength per unit solid angle])

$\overline{B}_j(T)$ Average blackbody spectral radiance over NOAA AVHRR Channel j (same units as $B_\lambda(T)$)

ε_λ Monochromatic emissivity (dimensionless [ ])

$\overline{\varepsilon}_j$ Average spectral emissivity over NOAA-7 AVHRR Channel j (dimensionless [ ])

I_λ Monochromatic radiance (same units as Planck emission B_λ)

$I_{\overline{\lambda}}^{obs,j}$ Satellite-observed spectral radiance for AVHRR Channel j (same units as I_λ)

k_λ Absorption cross-section $[L^2M^{-1}]$

λ Wavelength [L]

p Atmospheric pressure $[ML^{-1}T^{-2}]$

p_{sfc} Atmospheric surface pressure $[ML^{-1}T^{-2}]$

ρ Density $[ML^{-3}]$, or Cloud cover (dimensionless [ ]). Context should be very clear

$R_j(\lambda)$ Spectral response function (dimensionless [ ])

T Temperature, $[\Theta]$

T_{sfc} Surface skin temperature, $[\Theta]$

T_{Br} Satellite-measured brightness temperature, $[\Theta]$

$\mathcal{T}_\lambda(p)$ Monochromatic transmittance at wavelength λ, atmospheric pressure level p (dimensionless [ ])

$\mathcal{T}_{\overline{\lambda},j}(p)$ Spectral transmittance for NOAA-7 AVHRR Channel j, valid at atmospheric pressure level p (dimensionless [ ])

τ_λ Monochromatic optical depth (dimensionless [ ])

z Geometric height, [L]